

UNIVERSIDADE DE SÃO PAULO

INSTITUTO DE FÍSICA

MELHORAMENTO DE CÉLULAS SOLARES POLIMÉRICAS DE  
HETEROJUNÇÃO NO VOLUME ATRAVÉS DA IMPLANTAÇÃO  
IÔNICA DE OURO NA CAMADA DE PEDOT:PSS

DENNIS GERARDO BRENES BADILLA

ORIENTADOR: PROF. DRA. MARIA CECÍLIA SALVADORI

DISSERTAÇÃO DE MESTRADO APRESENTADA AO  
INSTITUTO DE FÍSICA PARA A OBTENÇÃO DO TÍTULO DE  
MESTRE EM CIÊNCIAS

BANCA EXAMINADORA:

PROF. DRA. MARIA CECÍLIA SALVADORI (IFUSP)  
PROF. DR. ADRIANO MESQUITA ALENCAR (IFUSP)  
PROF. VLADIMIR JESUS TRAVA AIROLDI (INPE)

SÃO PAULO

2014

**FICHA CATALOGRÁFICA**  
**Preparada pelo Serviço de Biblioteca e Informação**  
**do Instituto de Física da Universidade de São Paulo**

Badilla, Dennis Gerardo Brenes

Células solares poliméricas: melhora no desempenho através de implantação iônica de ouro na camada de PEDOT:PS. São Paulo, 2014.

Dissertação (Mestrado) – Universidade de São Paulo. Instituto de Física. Depto de Física Aplicada.

Orientador: Prof. Dra. Maria Cecília B. S. Salvadori

Área de Concentração: Física Aplicada

Unitermos: 1. Energia solar; 2. Células solares; 3. Polímeros (Materiais); 4. Nanopartículas; 5. Fotovoltaica orgânica.

USP/IF/SBI-001/2015

UNIVERSIDADE DE SÃO PAULO

INSTITUTO DE FÍSICA

IMPROVEMENT OF BULK HETEROJUNCTION SOLAR CELLS  
TROUGH AU ION IMPLANTATION INTO  
PEDOT:PSS LAYER

DENNIS GERARDO BRENES BADILLA

SUPERVISOR: PROF. DRA. MARIA CECÍLIA SALVADORI

DISSERTATION SUBMITTED TO THE PHYSICS INSTITUTE  
IN PARTIAL FULFILLMENT OF THE REQUIREMENTS FOR  
THE DEGREE OF MASTER IN SCIENCE

EXAMINING COMMITTEE:

PROF. DRA. MARIA CECÍLIA SALVADORI (IFUSP)  
PROF. DR. ADRIANO MESQUITA ALENCAR (IFUSP)  
PROF. VLADIMIR JESUS TRAVA AIROLDI (INPE)

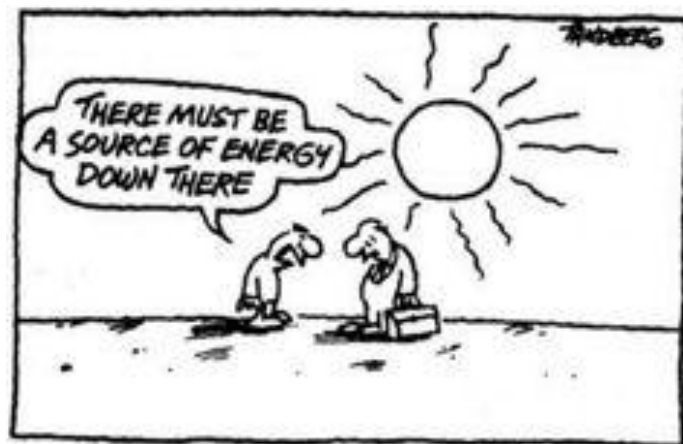
SÃO PAULO

2014



*To my parents, Sandra and Martín,  
and my two siblings, Derian and Ailyn,  
for their infinite encouragement and support.*

*To my journey's companion, Dani,  
for her innocent complicity and kind patience.  
As wrong as this may have resulted, it's ours.*





# ABSTRACT

Organic solar cells show great potential to become a commercially available technology for renewable clean energy production due to their attractive properties. Inexpensive materials and manufacturing processes, including classical roll-to-roll fabrication, as well as the ability to produce flexible, low weight, semitransparent devices are some of the advantages organic photovoltaics provide. Addressing the most common issues in these new technologies, i.e., the low efficiencies of devices and rapid degradation of materials, could bring a realistic alternative for the photovoltaic industry.

In this work, the performance of P<sub>3</sub>HT:PCBM based bulk heterojunction solar cells modified through low energy gold ion implantation in the hole transporting layer, the PEDOT:PSS, is studied. Reference solar cells without gold were also fabricated and characterized for comparison.

Through field emission scanning electron microscopy (FESEM) micrographs, the formation of gold nanoparticles (AuNPs) in the PEDOT:PSS has been shown layer for the highest implantation doses used. Absorbance measurements of PEDOT:PSS films before and after gold implantation further confirmed this result. TRIDYN and SRIM simulation

programs estimated shallow gold implantations of  $\sim 3$  nm underneath the PEDOT:PSS films surface.

Current-voltage ( $JxV$ ) characteristics of reference solar cells under AM 1.5 illumination presented the uncommon S-shaped curves, an abnormal deviation from typical  $JxV$  curves. This was attributed to PEDOT:PSS degradation due to oxygen and water exposure, which reduced its work function significantly. As a result, deteriorated parallel and series resistances were obtained in reference devices, which ultimately reduced their field factors and power conversion efficiencies. This abnormal behavior was consistently eliminated with the introduction of AuNPs near the PEDOT:PSS/Active-layer interface, leading to the rectification of the illuminated  $JxV$  curves of modified solar cells and the reestablishment of cell parameters. Consequently, outstanding improvements in the field factors and power conversion efficiencies were observed in these devices. This was attributed to enhancement (and prevention from the reduction) of the PEDOT:PSS work function layer due to the presence of AuNPs, which rearranged the energy levels at the interface to a more favorable state: higher electron blocking and lower hole extraction barriers.

# RESUMO

Células solares orgânicas têm mostrado grande potencial para se tornar uma alternativa tecnológica na produção de energia limpa e renovável. Baixo custo dos materiais e dos processos de manufatura, e a possibilidade de fabricar dispositivos com baixo peso, flexibilidade e semitransparência, inclusive pelo método clássico de *roll-to-roll*, são algumas das vantagens oferecidas pela fotovoltaica orgânica. Resolver os problemas mais comuns destes dispositivos, como a baixa eficiência na conversão de energia e a rápida degradação dos materiais, é necessário para sua disponibilização no mercado fotovoltaico atual.

Neste trabalho, células solares de heterojunção volumétrica baseadas no polímero P<sub>3</sub>HT e modificadas através da implantação de íons de ouro de baixa energia na camada de PEDOT:PSS são estudadas. Dispositivos equivalentes sem modificação de ouro também foram fabricados e caracterizados como referência.

Imagens obtidas através de um microscópio eletrônico de varredura por emissão de campo (FESEM – *Field Emission Scannig Electron Microscopy*) mostraram a formação de nanopartículas de ouro (AuNPs) na camada de PEDOT:PSS para as doses de implantação mais elevadas. Medidas do espectro de absorbância dos filmes de PEDOT:PSS antes e depois da implantação de ouro confirmam este resultado. Simulações feitas com os softwares

TRIDYN e SRIM estimaram o ouro implantado em uma profundidade de ~3 nm abaixo da superfície do PEDOT:PSS.

As curvas de corrente-tensão ( $J \times V$ ) características das células solares de referência sob iluminação AM 1.5 mostraram um comportamento de *forma S*, que corresponde a um desvio da forma típica das curvas  $J \times V$ . Isto foi atribuído à degradação dos filmes de PEDOT:PSS devido à exposição ao oxigênio e à água, que reduz sua função trabalho significativamente. Como resultado, deterioraram-se as resistências em paralelo e em série destes dispositivos, o que em última instância, reduziu o *Field Factor (FF)* e a eficiência na conversão de energia. Este comportamento anormal foi eliminado de forma consistente após a introdução de AuNPs perto da interface PEDOT:PSS/Camada-Ativa. As curvas  $J \times V$  das células solares modificadas sob iluminação foram retificadas e os valores dos seus parâmetros restabelecidos. Melhorias notáveis no *FF* e eficiência de conversão de energia foram obtidas para todas as células solares modificadas. Isto foi atribuído ao aumento da função trabalho da camada de PEDOT:PSS pela presença das AuNPs, que reorganizou os níveis de energia na interface para um estado mais favorável: com barreiras de potencial otimizadas para bloquear a extração de elétrons e favorecer a de buracos.



# ACKNOWLEDGMENTS

In order to finish this dissertation I acquired a lot of debts with many people. Here are some of them.

First, I'd like to thank my parents, Sandra and Martín, whose unconditional and endless support are beyond the limits any parent has ever given; gracias Ma! gracias Pa!

I am truly grateful to my supervisor, Prof. Dra. M. Cecília Salvadori, for the excellent guidance and helps of all sorts. Thanks for letting me be part of the *Laboratório de Filmes Finos*.

I'd like to thank Prof. Roberto M. Faria and Douglas Coutinho at the *Bernhard Gross* polymers group at the *Instituto de Física de São Carlos*, for the all the experimental and theoretical lessons in organic photovoltaics, and for providing all the facilities for my experiments. In São Carlos I am also thankful to Lilian, Marcos, Bruno and Niko for all the help offered.

I have acquired an enormous debt with the coworkers in the LFF. I thank Fernanda, Leonardo, Roman, Wagner, Sergio and Raissa for all the help, support and specially the

friendship offered during my time here. Thanks for everything guys. Specifically, I'd like to thank Raissa for the continuous portuguese lessons, the long talks in the office, the many rides home, etc. You became my best Brazilian friend menina, thank you for that.

I am grateful to all the people I met and the friends I made here in Brazil who made me feel at home. Particularly, I'd like to thank Fercho, David *el méshico*, Hans, Gina, Mera, my very good friend Abdur, Carlos *el Tino*, Marcia, don Victor Manotas and the rest for shaping this kind of international family we have. Thanks all for the good moments. We will meet again someday.

Of course, another member of this family to whom I owe much is my best friend Badi, whose constant encouragement and support kept me going even during the hardest times. Thank you bro for everything, you know how it is.

Also, I am grateful to my sister Ailyn and my brother Derian, who I've missed much during these years, for being part of that selected group of people that shapes my life. Gracias señorito y señorita!

Finally, I am infinitely grateful to Dani, my companion during this journey, who inevitably became the most important person in my life long time ago. For all your care, trust, love and support I'd like to say thanks. You've given me more that I will never be able to return.

# CONTENTS

ABSTRACT .....	vii
RESUMO .....	ix
ACKNOWLEDGMENTS.....	xii
LIST OF FIGURES.....	xvi
LIST OF TABLES.....	xxi
LIST OF SYMBOLS.....	xxii
INTRODUCTION .....	1
CHAPTER 1: CONJUGATED POLYMERS.....	6
1.1 ENERGY BAND STRUCTURE OF CONJUGATED POLYMERS.....	8
1.2 POLARONS, SOLITONS AND EXCITONS.....	12

<b>CHAPTER 2:</b>	<b>BASICS OF POLYMER SOLAR CELLS.....</b>	<b>15</b>
2.1	PHOTOINDUCED ELECTRON TRANSFER .....	17
2.2	BASIC DESIGN OF A POLYMER SOLAR CELL .....	18
2.3	WORKING PRINCIPLES .....	20
2.4	THE METAL-INSULATOR-METAL MODEL .....	23
2.5	CURRENT-VOLTAGE CHARACTERISTICS.....	24
2.6	IDEAL VS. REAL PHOTOVOLTAIC CELLS .....	26
2.7	METAL-SEMICONDUCTOR JUNCTION .....	28
2.8	DEVICE ARCHITECTURES .....	30
<b>CHAPTER 3:</b>	<b>EXPERIMENTAL DETAILS.....</b>	<b>35</b>
3.1	MATERIALS.....	35
3.2	ITO PHOTOLITHOGRAPHY AND SUBSTRATE PREPARATION .....	37
3.3	DEVICE FABRICATION .....	38
3.4	SOLAR CELLS CHARACTERIZATION .....	43
<b>CHAPTER 4:</b>	<b>RESULTS AND DISCUSSION.....</b>	<b>49</b>
4.1	RESULTS FROM RBS ANALYSIS .....	50
4.2	FESEM IMAGES.....	50
4.3	SRIM - TRIDYN SIMULATIONS .....	52
4.4	ABSORPTION MEASUREMENTS .....	53
4.5	CURRENT-VOLTAGE CHARACTERISTICS .....	54
4.6	COMPARATIVE ANALYSIS OF EXPERIMENTS A AND B .....	60
	<b>CONCLUSIONS.....</b>	<b>65</b>
	<b>APPENDIX: AFM IMAGES OF ITO/GLASS SUBSTRATES .....</b>	<b>67</b>
	<b>BIBLIOGRAPHY .....</b>	<b>70</b>

# LIST OF FIGURES

<b>Figure 1-</b> (a) World annual solar energy production since 2000 (GW) [ 4] (b) 2011 world total energy supply by source [ 5].	2
<b>Figure 2-</b> Best research solar cells efficiencies since 1975 and the groups where these results were obtained [ 13].	4
<b>Figure 3-</b> Structure of some common conjugated polymers and their conductivity values (adapted from [ 16]).	7
<b>Figure 4-</b> (a) Energy diagram for the $sp^3$ hybridization process; (b) final geometric arrangement of the of $sp^3$ orbitals; (c) $\sigma$ (top) and $\pi$ (bottom) bonds formation. (Adapted from [ 17]).	8
<b>Figure 5-</b> (a) Lewis diagram for the resonance structures of benzene ( $C_6H_6$ ); (b) $\sigma$ bonds between $sp^2$ orbitals in it; (c) $2p_z$ orbitals available to participate in the $\pi$ bonds; (d) equivalent forms to make $\pi$ bonds; (e) delocalization of the electrons within the molecule; (f) Lewis representation of the delocalized electrons. (Adapted from [ 17]).	9
<b>Figure 6-</b> Band structure of a conjugated polymer when: (a) Franck-Condon like ionization occurs; (b) a polaron, (c) two polarons, (d) a bipolaron and (e) bipolaron bands are formed. The dotted line represents the Fermi level.	13

**Figure 7-**(a) Degeneracy of the ground state geometry of trans polyacetylene; (b) schematic illustration of the geometric (top) and band (bottom) structure of a neutral (center), positive (right) and negative (left) soliton on a trans polyacetylene chain (adapted from [ 23]); (c) singlet exciton . ..... 14

**Figure 8-** (a) Illustration of the photoinduced charge transfer from P<sub>3</sub>HT to PCBM (adopted from [ 36]); (b) sketch of energy diagram for the process. The band offset between the two materials provides an exothermic way for dissociation of excitons. .... 17

**Figure 9-** Basic design of a polymer solar cell. Light enters the device through a transparent substrate and is absorbed in the active layer, which imposes the requirement of transparency on the anode and hole transporting layer (HTL). The HTL, along with the electron transporting layer (ETL), improve the overall performances of organic solar cells, enhancing charge transport throughout the device. Nevertheless, their use is optional. The anode and cathode collect the photogenerated charges and introduce them to an external circuit..... 19

**Figure 10-** Absorption coefficients of a few organic materials commonly used in the active layers of photovoltaic cells. For comparison, standard AM 1.5 terrestrial solar spectrum is included (Adopted from [ 36]). ..... 20

**Figure 11-** Depiction of the MIM model applied to a photovoltaic cell in different regimes: (a) short circuit condition: photogenerated charge carriers drift towards the electrodes under illumination; (b) open circuit condition: no current flow, (c) reverse bias: photogenerated charges drift in strong electric fields; (d) forward bias larger than  $V_{oc}$ : injected charge current flows. The HOMO and LUMO bands of the semiconductor, as well as the Fermi levels of the metals, are indicated. (Adopted from [ 38]) ..... 23

**Figure 12-** Typical *Current – Voltage* characteristics of a solar cell in the dark and under illumination. The short circuit current  $J_{sc}$  and open circuit voltage  $V_{oc}$  are indicated. Maximum power output of the cells is at the point  $(V_m, J_m)$ , denoted by the dotted rectangle (adopted from [ 34]). ..... 25

**Figure 13-** Equivalent circuit of an (a) ideal and (b) real organic solar cells showing the total current  $J$ , the photogenerated current  $J_{ph}$  and the diode dark saturation current  $J_o$ . The latter also shows the series and parallel resistances,  $R_s$  and  $R_p$ . Other resistors, capacitors and diodes can be added to model more complex behaviors. .... 26

**Figure 14-**  $JxV$  characteristics for an ideal and real solar cell. Ideal cell's curve possesses a much higher field factor than the real cell, as can be deduced from the "squareness" of the curves.....27

**Figure 15-** M/S junction formation for an  $n$ -type semiconductor. Metal's:  $\Phi_M$  = work function,  $E_{FM}$  = Fermi level; Semiconductor's:  $\chi$  = electron affinity,  $\phi_S$  = work function,  $E_c$  = conduction band,  $E_v$  = valence band,  $E_{FS}$  = Fermi level,  $E_i$  = intrinsic Fermi level;  $E_o$  = vacuum level,  $E_F$  = equilibrium Fermi level,  $\phi_B$  = potential barrier blocking electron flow from M to S,  $\phi_{BS}$  = potential barrier from S to M,  $w$  = depletion region depth. A Schottky barrier (b) is formed when  $\Phi_M > \Phi_S$  (a); an ohmic contact (d) is formed when  $\Phi_M < \Phi_S$  (c)..... 29

**Figure 16-** Monolayer cell viewed under the: (a) MIM model, short circuit conditions; (b) Schottky junction, where a Schottky barrier forms at the aluminum electrode and an ohmic contact at the Au. VB = valence band, CB = conduction band,  $E_g$  = bandgap,  $P^+$  and  $P^-$  = positive and negative polarons. (Adopted from [ 40] and [ 38], respectively) ..... 31

**Figure 17-** Depiction of a planar bilayer heterojunction. Photogenerated exciton can only be dissociated in a thin layer at the heterojunction interface. (Adopted from [ 38]).....32

**Figure 18-** Bulk heterojunction solar cell: (a) energy levels diagram (Adopted from [ 38]); (b) ordered ideal design of the active layer. Photogenerated exciton can be dissociated throughout the whole active layer..... 33

**Figure 19-** Energy level diagram of the bulk heterojunction solar cells fabricated in this work. .... 36

**Figure 20-** Photolithography procedure performed on the ITO/glass substrate; (a) ITO/glass substrate before photolithography, (b) spin casted photoresist on ITO, (c) UV exposition of photoresist through a mask, (d) developed photoresist pattern, (e) etched ITO layer still with photoresist, (f) ITO electrodes array on glass, consisting of two ground contacts (rectangles) and six electrodes for solar cells. ....37

**Figure 21-** (a) Outline of the layer structure forming solar cells on substrates used in this work; (b) Diagram showing the intersection between the ITO and metal contacts on one substrate, which defines the effective area of each solar cell. There are six solar cells and two ground contacts on each substrate. .... 40

**Figure 22-** (a) top view of masking process of the PEDOT:PSS film on ITO/glass substrate for ion implantation. Only 3 of 6 solar cells are modified during this procedure; (b) Schematic diagram of the low vacuum arc plasma deposition system (Adopted from [47]). ..... 41

**Figure 23-** Final architecture of the layers forming the modified and non-modified solar cells investigated in this work..... 42

**Figure 24-** Electron beam interaction volume inside the material. Secondary and back-scattered electrons, as well as characteristic X rays are signals generated within different regions inside the sample. .... 44

**Figure 25-** example of altitude profile created by Dektak II profilometer from VEECO, used for measuring thickness of polymer and metal layers in this work. .... 45

**Figure 26-** RBS spectrum of gold implanted Si substrates obtained during RBS analysis (black) and RUMP simulation used for analysis (red). .... 46

**Figure 27-** Solar radiation spectrum: right outside earth's atmosphere (AM 0) and at a point on the earth's surface where, having entered the atmosphere at an certain angle, the sunlight had crossed 1,5 atmospheres (AM 1.5). (Adopted from [ 53]) ..... 47

**Figure 28-** Definition of air mass coefficient AM. Sunlight entering the earth's atmosphere in angle can travel for a path length equivalent to more than 1 atmosphere (Adopted from the web). .... 48

**Figure 29-** FESEM micrographs of PEDOT:PSS coated ITO substrates: (a) before implantation; and after implantation of dose: (b) B1 ( $2.1 \times 10^{15}$  atoms/cm<sup>2</sup>), (c) A1 ( $3.1 \times 10^{15}$  atoms/cm<sup>2</sup>), (d) A2 ( $6.4 \times 10^{15}$  atoms/cm<sup>2</sup>) and (e) B2 ( $9.1 \times 10^{15}$  atoms/cm<sup>2</sup>). Formation of gold nanoparticles for implantation values  $\geq 3.1 \times 10^{15}$  atoms/cm<sup>2</sup> (c) is noticeable. Density of these AuNPs increases as implantation dose is enhanced, as seen in (d) and (e). The white bar represents 400 nm length..... 51

**Figure 30-** Depth profile of Au implanted PEDOT:PSS for the ion energy of 49 eV and doses used in this experiment, as calculated by the TRIDYN simulation code. ....52

**Figure 31-** (a) Absorbance measurements of PEDOT:PSS films over ITO coated glass before (pristine PEDOT:PSS) and after gold implantation for several doses; (b) each of the curves presented in (a) minus the baseline curve (Pristine PEDOT:PSS line); which gives the absorbance of the implanted gold nanostructures alone. ....53

**Figure 32-**  $JxV$  characteristics for reference solar cells from experiments A and B: (a) in the dark (inset shows the semi-log scale); (b) under AM 1.5 illumination. Significant differences in photovoltaics parameters from experiments are evident. ....55

**Figure 33-** Typical  $JxV$  characteristics for modified and reference devices from experiment A: (a) in the dark; (b) under AM 1.5 illumination. Gold-implanted solar cells show better overall performance in comparison with control cells.....57

**Figure 34-** Typical  $JxV$  characteristics of control and modified solar cells from experiment B: (a) in the dark; (b) under AM 1.5 light. As in experiment A, AuNPs rectify the poor shape presented in illuminated  $JxV$  curves in control cells. As will be discussed in section 4.6, this poor shaped  $JxV$  are called S-shaped curves; which origins are analyzed. .... 59

**Figure 35-** Similar results involving gold on PEDOT:PSS were obtained by Ardestani et al for CuPc:Fullerene based bilayer solar cells<sup>60</sup>. Degrading effects of oxygen and moisture on the  $JxV$  characteristics of: (a) bilayer control solar cells; (b) Solar cell modified with an Au thin film in the PEDOT:PSS/Active-layer interface. S-shaped  $JxV$  in (a) are attributed to degradation of the PEDOT:PSS/Active-layer interface due to water diffusion into PEDOT:PSS. The gold thin film at the interface rectified the S-shape of the  $JxV$  and dramatically decelerated the degradation process. .... 62

**Figure 36-** Energy band diagram of the process BHJ solar cells went through during these experiments, for the case of : control cells (with pristine PEDOT:PSS), which work function degrades upon air exposition (red arrow); and with modified PEDOT:PSS (with embedded AuNPs), which work function is rectified (green arrow). .... 63

**Figure 37-** (a) Outline of the SPM working loop (Adopted from [ 80]); (b) AFM tapping mode operation principle; (c) diagram of the ITO/glass samples analyzed in this experiment. .... 68

**Figure 38-** 2  $\mu\text{m}$  x 2  $\mu\text{m}$  AFM tapping scans of ITO samples for roughness analyses..... 69

# LIST OF TABLES

<b>Table 1-</b> Generalization of the M/S work function relationships for the appearance of Schottky and ohmic contacts, for both <i>n</i> and <i>p</i> type semiconductors. ....	30
<b>Table 2-</b> Gold implantation doses implemented in this work. The number of references as well as modified cells for each dose is showed. ....	42
<b>Table 3-</b> Average results obtained for modified and references solar cells parameters for experiment A. Outstanding improvements for devices with AuNPs are manifest. ....	58
<b>Table 4-</b> Average results obtained for modified and references solar cells parameters for experiment B. Although the values are quite different, relative performance between experiment A and B is pretty similar. ....	59

# LIST OF SYMBOLS

$\alpha$	absorption coefficient
$\psi$	wave function of a molecular state
$\sigma$	covalent bond with electronic density along the internuclear axis of binding atoms
$\pi$	covalent bond with electronic density above and below the internuclear axis
$E_g$	energy band gap
$h$	Planck's constant
$\hbar$	Planck's constant/ $2\pi$
$m_e$	electron mass
$m_h$	hole mass
$\epsilon$	dielectric constant
$k_B$	Boltzmann's constant
$T$	absolute temperature
$E$	electric field
$U$	electric potential
$L_{ex}$	exciton diffusion length
$\mu$	chemical potential energy
$\mu_n$	electron mobility
$E_F$	energy of the Fermi level

$J_n(x)$	general form of current density charge carrier
$n(x)$	charge carrier concentration
$\eta$	power conversion efficiency
$FF$	field factor
$J$	current density
$J_{ph}$	photocurrent density
$V_{oc}$	open circuit voltage
$J_{sc}$	short circuit current
$V$	applied voltage
$P$	power
$J_D$	diode current density
$J_o$	diode saturation current
$\phi_M$	metal's work function
$\phi_S$	semiconductor's work function
$\phi_{BS}$	Schottky barrier
$\phi_B$	Schottky barrier (metal to semiconductor)
$R_p$	parallel resistance
$R_s$	series resistance
$E_c$	conduction band
$E_v$	valence band
$E_o$	vacuum level
$w$	depletion region depth
$\chi$	electron affinity
$D$	electron donor
$A$	electron acceptor
$I_o$	intensity of incident light
$Tr$	transmission
$\theta_z$	zenith angle
$l$	light's path length through the atmosphere
$l_o$	equivalent length of one atmosphere

# INTRODUCTION

During 2012 the world total energy consumption reached the 18 TW limit <sup>1,2</sup>. Of this, over 80% were generated from fossil fuels <sup>1,3</sup>. Apart from being non-renewable resources, fossil fuels produce carbon emissions that are largely responsible for global warming. According to the International Energy Agency's special report *Redrawing the Energy Climate Map*, "global energy-related carbon-dioxide (CO<sub>2</sub>) emissions increased by 1.4% to reach 31.6 gigatonnes (Gt) in 2012, a historic high" <sup>3</sup>. In this report, the agency also pointed out that "in may 2013, CO<sub>2</sub> levels in the atmosphere exceeded 400 parts per million for the first time in several hundred millennia". Due to the growing of global economies, including the ones from emerging countries such as Brazil, India and China, along with the estimated increase in world population, a 50% increment in the global energy demand is expected by 2035 - 2040 <sup>1,2</sup>. Is evident that major changes in the ways energy is produced are needed, as we cannot continue *doing business as usual*. The implementation of new energy policies that stimulate the development of clean, renewable energy is essential for the sustainability of our ecosystems. In providing the means for this enterprise, technological and scientific production must be held accountable.

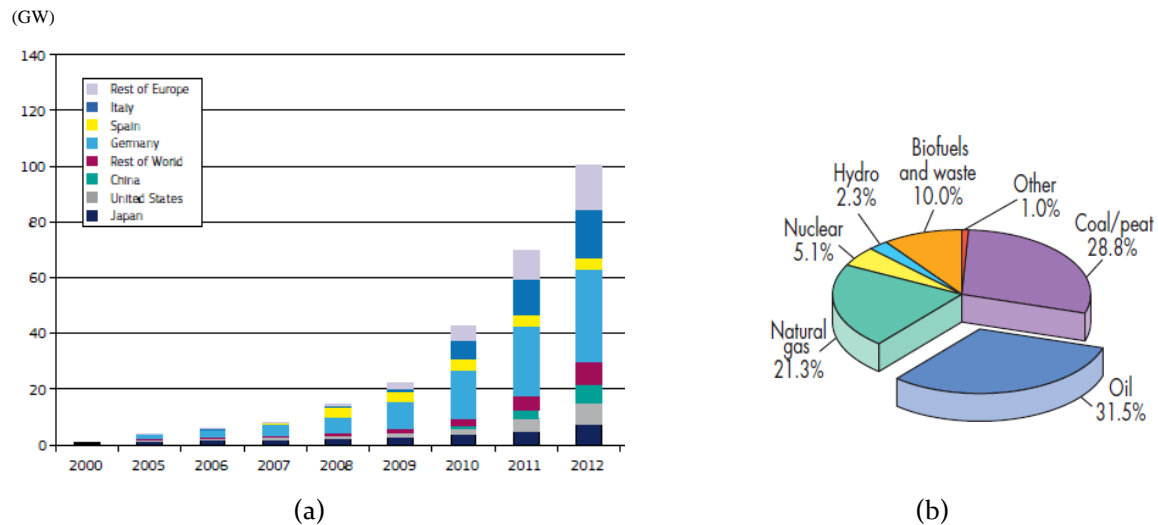


**Figure 1-** (a) World annual solar energy production since 2000 (GW); (b) 2011 world total energy supply by source. Adopted from (a) 4 and (b) 5.

Within this context, sunlight emerges as the most viable option to be used as the primary source of clean energy, ahead of others such as nuclear or hydroelectric energies, for a variety of reasons: it is the most abundant energy resource on the planet; is fairly distributed across most of the earth's surface, which make it secure from geopolitical constraints (theoretically at least!); it can be converted into electricity without producing pollutants (greenhouse gases or toxic residues) and it is basically inexhaustible. On average,  $1,2 \times 10^5$  TW of solar energy reach the earth's surface, which means that in one hour the sun delivers more energy in our planet than humans consume in one year<sup>6</sup>. It is clear that a more efficient utilization of this resource can ensure the sustainable energy future we seek.

Figure 1(a) shows the evolution of solar energy production since 2000<sup>4</sup>. Annual increments between ~40% and ~80% make of photovoltaics one of the fastest growing industries in the world. Nevertheless, the contribution of solar energy to the global energy demand is almost negligible at present day, as shown in Figure 1(b). It exhibits the 2011 world total primary energy supply distribution by source<sup>5</sup>, which includes the photovoltaic energy in the "other" section, along with geothermal and wind energies, for a combined share of 1%. In other words, despite the intense growing, solar energy industry represents less than 1% of today's total energy production. The reason is pretty straightforward: as to present time, solar energy production is too expensive. The photovoltaic market is overwhelmingly

dominated by wafer-based crystalline silicon solar cells mainly due to its efficiency<sup>i</sup>, and they are responsible for over 85% of the total photovoltaic production<sup>4</sup>. Other inorganic semiconductors such as gallium-arsenide (GaAs) and cadmium-telluride (CdTe) are implemented in solar devices to a much lesser extent. Yet, the high cost of these materials and the complexity of the fabrication processes, as well as the high cost of components for getting the electricity from the modules, are factors that increase the final cost of the photovoltaic kilowatt up to a point where is no longer attractive in the energy market. Still, countries like China, Taiwan and Japan in Asia, or Germany in Europe, continue to invest intensively in photovoltaic generation trying to diminish their carbon footprint on the planet<sup>4</sup>.

An enormous amount of effort has been put together within the scientific community in finding more efficient ways to exploit the sunlight resource. Some of the approaches involve inorganic thin-films<sup>7</sup>, quantum dots<sup>8</sup>, copper-zinc-tin-X (CZTX)<sup>ii</sup> compounds<sup>9,10</sup>, perovskite compounds<sup>11</sup> and organic materials<sup>12</sup>. Due to a number of reasons, organic solar cells, also referred as plastic solar cells, show great potential to become a commercially available technology for renewable energy production. Inexpensive materials and manufacturing processes, flexibility and low weight, solution processability, semitransparency and facile chemical tailoring are some of the attractive properties organic photovoltaics (OPV) provides.

In Figure 2 the evolution of best research cells efficiencies since the mid seventies, according to the US National Renewable Energy Laboratory (NREL)<sup>13</sup>, is shown. Although OPV efficiencies appear in the lower part of the chart, is evident that great progress has been made in the last decade, turning the promises into more realistic goals. Furthermore, different printing and coating processes have been developed and classical roll-to-roll processing of organic solar cells has been achieved<sup>14</sup> for polymer solar cells, a type of OPV device, that shows how OPV “are unrivalled in terms of processing cost, processing speed, processing simplicity and thermal budget” and how polymer devices may be “the only photo-voltaic technology [sic] that potentially offers a convincing solution to the problem of

---

<sup>i</sup> For solar cell efficiencies data see Figure 2.

<sup>ii</sup> X=sulfur, selenide or sulfure-selenide alloy.

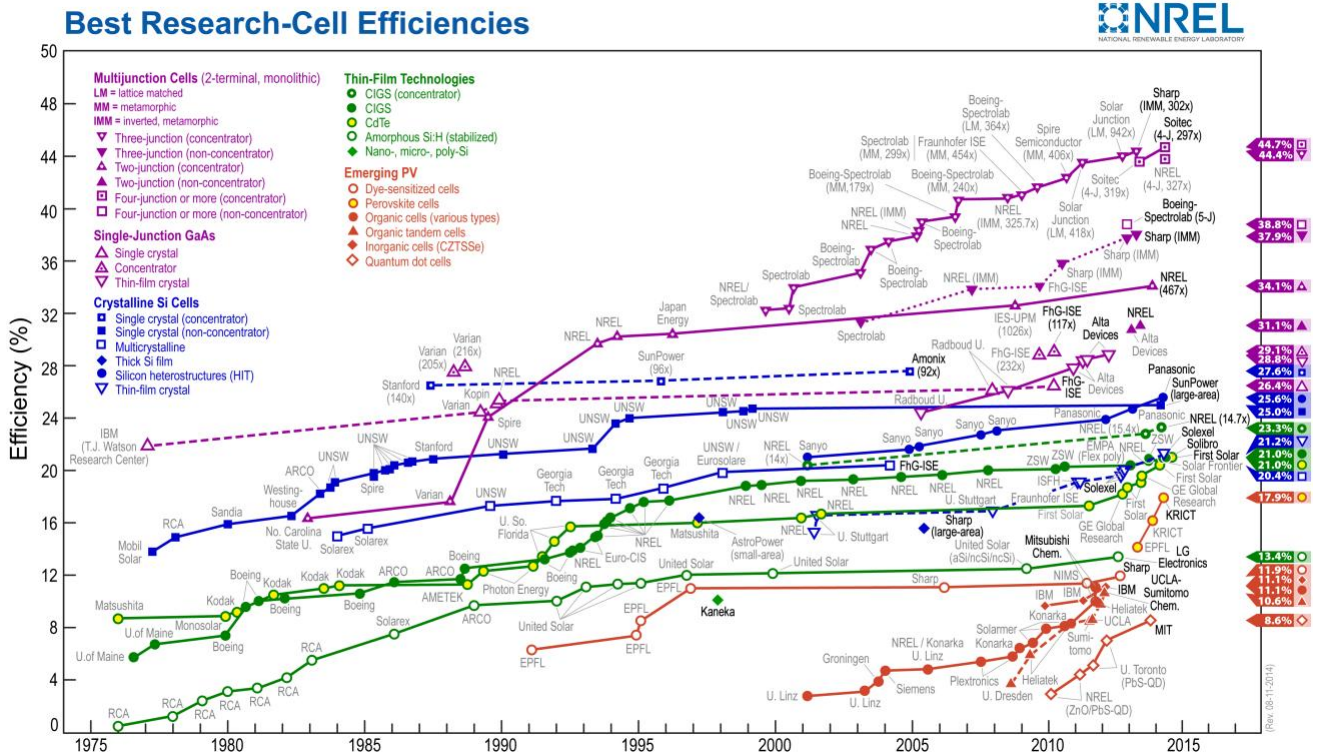


Figure 2- Best research solar cells efficiencies since 1975 and the groups where these results were obtained [ 13].

a high cost commonly encountered for photo-voltaic technologies”<sup>iii</sup>. However, there are still drawbacks in OPV that need to be overcome. Rather low efficiencies, poor operational stability and degradation of the devices are the major ones. Addressing these issues intense research is currently being conducted from most scientific domains.

Recently, the thin films group at the *Instituto de Física da Universidade de São Paulo*, the *Laboratório de Filmes Finos (LFF)*, got involved in the OPV research field as part of a bigger Brazilian project, the National Institute of Science and Technology for Organic Electronics (INEO). INEO is a national multidisciplinary research network aiming “to place Brazil in a good position with regard to the fundamental science and applications in organic electronics”<sup>iv</sup> combining fundamental research with technological developments. The LFF, in association with the *Bernhard Gross* polymers group at the *Instituto de Física de São*

<sup>iii</sup> Prof. Frederik Krebs, head of the Department of Energy Conversion and Storage of the Technical University of Denmark [ 14].

<sup>iv</sup> INEO website: [www.ifsc.usp.br/~ineo/english/theinstitute/](http://www.ifsc.usp.br/~ineo/english/theinstitute/); accessed on september 9<sup>th</sup>, 2014.

*Carlos*, is developing a project on OPV that involves the fabrication, characterization and analysis of organic solar cells made of conjugated polymers (see chapter 2). This dissertation is a partial result of such project.

In this work we study the performance of bulk heterojunction polymer solar cells, a type of organic solar cell, and make use of the facilities in our lab to introduce gold nanoparticles into the cells to improve its performances. For comparison, references and modified solar cells are analyzed. The effects of gold nanoparticles in the cells are investigated.

# CHAPTER 1

## CONJUGATED POLYMERS

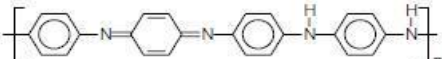
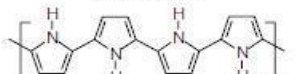
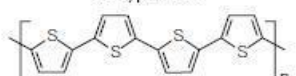
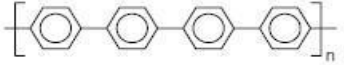
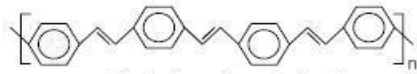
The first investigations in organic photovoltaics started approximately in the 1950s with the study of some common dyes, such as methylene blue, and the implementation of its semiconducting properties to photovoltaic devices. Nonetheless, the field didn't gain much attention until the late 1970s. With the use of small organic molecules (pigments) and specially, with the (allegedly accidental) discovery of conducting polymers<sup>v</sup> in 1977<sup>15</sup> the interest in OPV was rekindled. Shirakawa and his colleagues observed that conductivity of polyacetylene increased from  $10^{-8} \text{ S}\cdot\text{cm}^{-1}$  to  $10^3 \text{ S}\cdot\text{cm}^{-1}$  after doping it with iodine<sup>vi</sup>. These materials were incorporated in OPV producing significant improvements within past years.

A polymer is a large molecule chain composed of a multiple repeated fundamental unit, called monomer, covalently bonded throughout the chain. Inexpensive and simple manufacturing processes have allowed the exploitation of the broad range of properties polymers offer, making them quite abundant in the everyday life. The idea of associating its

---

<sup>v</sup> More precisely, intrinsically conducting polymers. See next page.

<sup>vi</sup>. "For the discovery and development of conductive polymers" they were awarded the Nobel Prize in chemistry in 2000.

Conductive polymer	Conductivity (S <sub>cm</sub> <sup>-1</sup> )
 Polyacetylene	10 <sup>3</sup> - 10 <sup>6</sup>
 Polyaniline	10 - 10 <sup>3</sup>
 Polypyrrole	600
 Polythiophene	200
 Poly(p-phenylene)	500
 Poly(p-phenylene vinylene)	1

**Figure 3-** Structure of some common conjugated polymers and their conductivity values (adapted from 16).

mechanical properties to the electrical properties of metals goes back to the 1950s, when conductive materials such as metallic fibers or soot particles were incorporated to the polymeric matrix, enhancing its conductivity of up to 10 S·cm<sup>-1</sup>. These polymers, referred as *extrinsically* conductive polymers<sup>16</sup>, were shown to obey the Ohm's law. The later discovery of the *intrinsically* conductive polymers, those able to reach metallic-like electrical conductivity through oxidation-reduction reactions (called "doping", in analogy to the inorganic semiconductors), showed there is no reason why polymers can't conduct electricity.

Intrinsically conductive polymers are known better as conjugated polymers, because they are characterized by a backbone chain of alternating double-single bonds between the carbon atoms. This alternation enables an electron flux throughout the chain, as will be discussed on the next section. Figure 3 shows some of the most common conjugated polymers and their approximate conductivity values. As reference, good conductor metals such as copper or gold possess conductivities of the same order as polyacetylene.

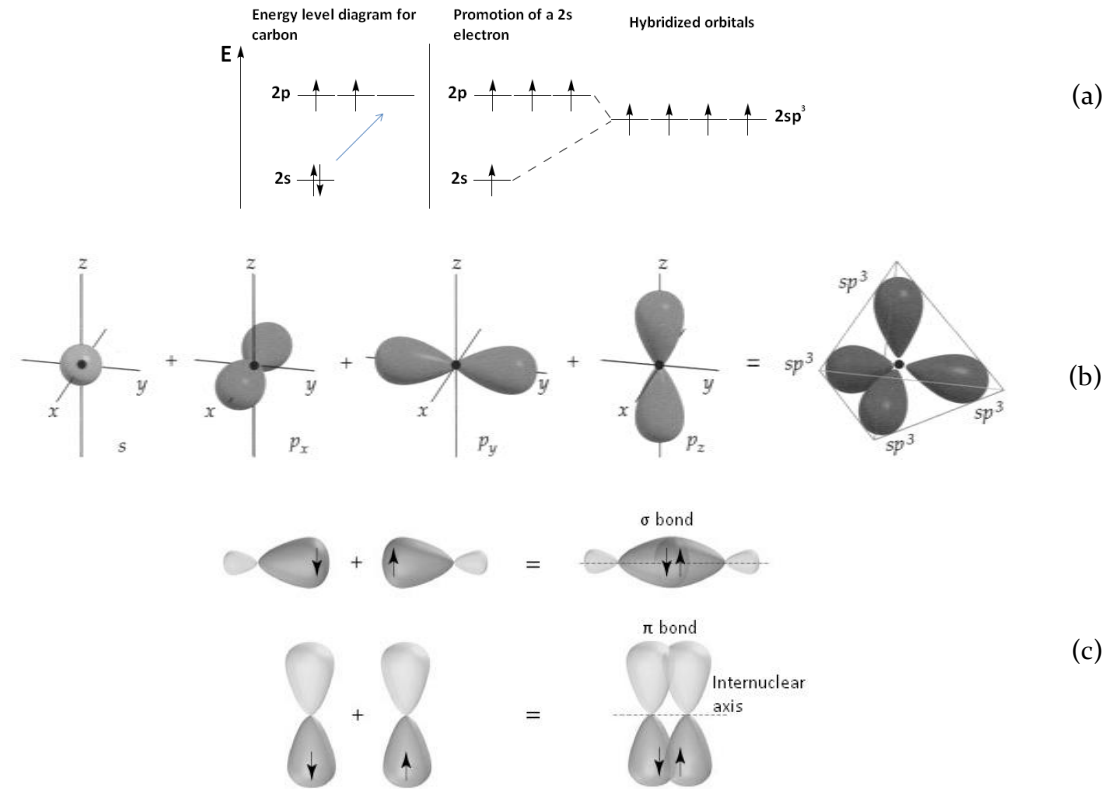


**Figure 4-** (a) Energy diagram for the  $sp^3$  hybridization process; (b) final geometric arrangement of the of  $sp^3$  orbitals; (c)  $\sigma$  (top) and  $\pi$  (bottom) bonds formation. (Adapted from 17).

### 1.1 ENERGY BAND STRUCTURE OF CONJUGATED POLYMERS

The electronic structure of carbon in the ground state is  $1s^2 2s^2 2p^2$ , which enables carbon atoms to form up to four chemical bonds through the hybridized valence shells  $sp$ ,  $sp^2$ , and  $sp^3$ ; along with the  $p_z$  atomic orbital. The hybridization process for  $sp^3$  orbitals is outlined in Figure 4(a) and (b). One electron from the full  $2s$  shell is promoted to the only  $2p$  state available, allowing the combination of all four half filled atomic orbitals into four energetically equivalent  $sp^3$  orbitals (Figure 4(a)). These orbitals can be depicted as large lobes pointing toward a vertex of a tetrahedron (4(b)), a geometrical arrangement that allows the formation of only one type of covalent bonds, the  $\sigma$  bonds, with other atoms.  $\sigma$  bonds are strong covalent bonds characterized by having the electronic density along the internuclear axis of the two binding atoms (4(c)-top). Non-conducting polymers such as polyethylene are characterized by these hybridized  $sp^3$  states.

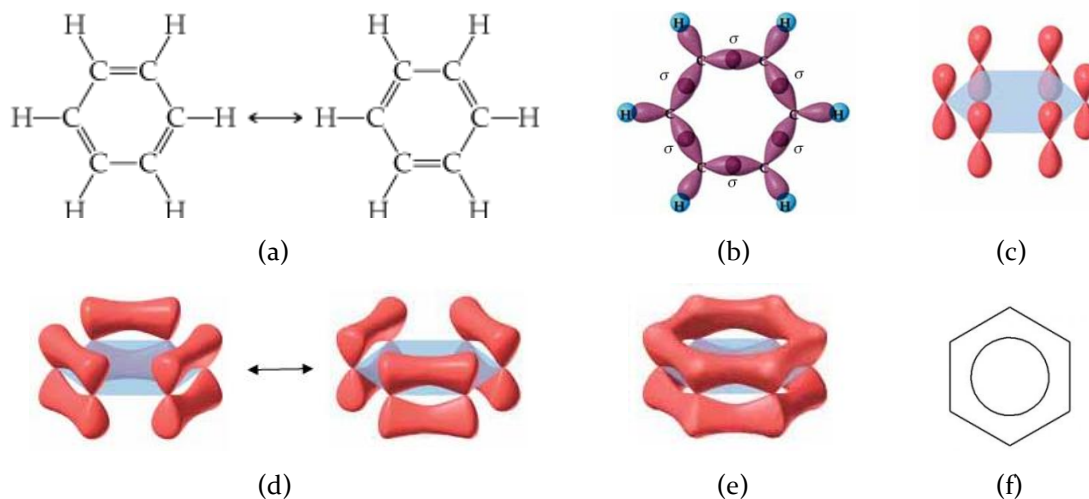


**Figure 5-** (a) Lewis diagram for the resonance structures of benzene ( $C_6H_6$ ); (b)  $\sigma$  bonds between  $sp^2$  orbitals in it; (c)  $2p_z$  orbitals available to participate in the  $\pi$  bonds; (d) equivalent forms to make  $\pi$  bonds; (e) delocalization of the electrons within the molecule; (f) Lewis representation of the delocalized electrons. (Adapted from 17).

On the other hand, the  $sp$  and  $sp^2$  hybridized states, present in conjugated polymers, continue to possess  $p_z$  atomic orbitals after hybridization. This permits the formation not only of  $\sigma$  bonds, but also of a different kind of covalent links known as  $\pi$  bonds. Unlike the former, the electronic density in  $\pi$  bonds is located above and below the internuclear axis (Figure 4(c)-bottom), what makes them a weaker type of link. The  $\pi$  bonds take place when double or triple covalent bonds are formed, and exhibit delocalized electrons in molecules with resonance structures. For example, the benzene molecule,  $C_6H_6$ , is well known for having resonance structures (Figure 5(a)) with exchanged positions of single (C-C) and double (C=C) carbon-carbon bonds in them. Figure 5(b) shows the  $sp^2$  hybridized carbon orbitals making  $\sigma$  bonds in the C-C and one of every C=C, as well as in C-H (unlabeled). Perpendicular to the plane of  $sp^2$  orbitals there is one  $2p_z$  orbital per atom available for the remaining bonds in each C=C (Figure 5(c)). Due to the resonance structures, there are two possible ways of making these  $\pi$  bonds between  $2p_z$  orbitals, as shown in Figure 5(d). However, experimental measurements showed that the six carbon-carbon bonds in benzene have the same length,  $\sim 1.40 \text{ \AA}$ , intermediate between the C-C and the C=C lengths. Instead of a resonance structure, this confirms the delocalization of the electrons across the six carbon atoms of the molecule through the  $\pi$  bonds (Figure 5(e)). The circle inside the hexagon in the usual benzene depiction represents this delocalization (Figure 5(f)).

By the quantum mechanical requirements of indistinguishability, overlapping of two wave functions of identical atoms leads to the splitting of energetically equivalent atomic orbitals into two distinct energy levels. Combination of ground state orbitals of hydrogen atoms A and B, for example, results in molecular states that are linear combinations of atomic orbitals<sup>vii</sup>, defined as:

$$\psi_{\sigma} = \psi_{1s}(r_A) + \psi_{1s}(r_B), \quad \psi_{\sigma^*} = \psi_{1s}(r_A) - \psi_{1s}(r_B) \quad (1.1)$$

where  $\psi_{1s}(r_A)$  and  $\psi_{1s}(r_B)$  are the ground state wave function of hydrogen atoms A and B, and  $\psi_{\sigma}$  and  $\psi_{\sigma^*}$  correspond to the bonding and anti-bonding molecular orbitals, respectively. Quantum mechanical calculations show that the energy levels of these states are such that  $E_{\sigma} < E_{\sigma^*}$ , which means electrons occupy bonding states first. The same applies for higher energy atomic orbitals.

As we go to a system containing  $N$  identical atoms (of any given species), each energy level of the atoms splits into a set of  $N$  levels as the atoms are brought together and orbitals overlap. The closer the atoms are, the bigger the spread in energy of a particular orbital, since the separation distance between the atoms specifies the amount of overlap that causes the splitting. In the case of solids, where atoms are just a few angstroms from one another, the energy spread is of the order of some electron volts. Since the number of atoms in a solid is of the order of  $\sim 10^{23}/\text{cm}^3$ , the spread energy levels are so extremely close to each other that are said to form a continuous energy band.

In conjugated polymers, the  $\sigma$  and  $\pi$  covalent bonds formed between carbon atoms correspond to the  $\psi_{\sigma}$  and  $\psi_{\pi}$  bonding molecular orbitals generated by the overlapping of the atomic orbitals  $sp^2$  (or  $sp$ ) states and  $2p_z$ , respectively. Evidently, higher energy anti-bonding levels  $\psi_{\sigma^*}$  and  $\psi_{\pi^*}$ , or simply  $\sigma^*$  and  $\pi^*$ , are also generated. The existence of  $\pi$  and  $\pi^*$  orbitals in the alternating C-C and C=C bonds throughout long polymeric chains leads to the complete delocalization of the electrons within the chain. In this sense, essentially continuous energy levels are created by  $\pi$  and  $\pi^*$  states in conjugated polymers. The  $\pi$  levels are characterized for being the *highest occupied molecular orbitals* (HOMO), which is the

---

<sup>vii</sup> According to *the linear combination of atomic orbitals* (LCAO) method, a quantum mechanical approximation that can be extended to more complicated molecules.

polymeric equivalent of valence band in inorganic semiconductors. The anti-bonding  $\pi^*$  levels are the *lowest unoccupied molecular orbitals* (LUMO), and act as the conduction band. The energy gap  $E_g(\pi)$  between the HOMO and LUMO is small enough ( $\sim 2-4$  eV) to allow low energy excitations and semiconductor behavior in conjugated polymers.

The disordered nature of polymers also plays a significant role in the energy band structure of conjugated polymers. Delocalization of electrons in the  $\pi$  levels is limited by the morphology of the polymeric structure to a definite length known as a *conjugation length*. These segments, which are separated by defects or twists in the polymeric chain, are characterized by an energy band gap  $E_g(\pi)$  that depends on the length  $L$  of the segment. One of the simplest models for the energy band structure of conjugated polymers, the *Free Electron* (FE) model<sup>18</sup>, shows that  $E_g(\pi)$  decreases as  $L$  increases. According to this model, the band gap is given by:

$$E_g(\pi) = \frac{\hbar^2 \pi^2}{2m_e L^2} (N + 1) \quad (1.2)$$

where  $\hbar$  is the reduced Plank constant,  $m_e$  is the electron mass,  $L=Na$  is the length of the polymer segment; with  $N$ =number of delocalized  $\pi$ -electrons, and  $a$ = averaged bond length. This gives the  $1/N$  trend for the energy gap in finite segments of conjugated polymers, i.e., smaller  $E_g(\pi)$  for larger  $L$ . This prediction, besides confirming the semiconductor behavior of conjugated polymers, is “*a posteriori* confirmation that  $\pi$ -electrons are delocalized along a straight section”<sup>18</sup> within them. The FE model, however, fails to predict the saturation gap in the asymptotic limit  $N \rightarrow \infty$ , as  $E_g(\pi)$  goes to zero. For this, is necessary to take into account the (alternating) bonding structure of conjugated polymers. Such approach is followed in the more general, but also more complex, *Hückel molecular orbital* method<sup>18</sup>. This model correctly retrieves the semiconducting behavior of conjugated polymers in the general case.

As in inorganic semiconductors, conjugated polymers are doped (oxidized or reduced) to improve their semiconducting behavior, although significant differences in the doping process are evident. One major distinction is the quantity of doping material used during the processes, as large amounts of it are incorporated in conjugated polymers, accounting for up to the 50% of the total mass of the composite in some cases. But perhaps the most remarkable difference with inorganic semiconductors is the reversible nature of

the doping process in polymeric case, meaning they can move back and forth the insulating and conducting states as a function of doping material incorporated. This feature interested researchers due to the possibility of having a variable band gap semiconductor that can be controlled through addition/removal of dopant agents.

## 1.2 POLARONS, SOLITONS AND EXCITONS

Conjugated polymers can be considered essentially quasi one dimensional structures because covalent bounding within the polymeric chain is much stronger than Van der Waals interactions between chains. Also, as occurs in other organic molecules, the equilibrium geometry of the structure depends on its ionic state and can be different from that in the ground state. These two characteristics are responsible for unusual nature of charge carriers present in these materials. It was demonstrated that conduction in conjugated polymers is associated with spinless charge carries rather than unpaired electrons or holes<sup>19-21</sup>. In order to explain this, a quasi particle model of coupled charge-lattice deformations that are “self-localized” in the chain was implemented<sup>23</sup>. These quasi particles can be generated in the polymer from various processes such as structural defects formation during polymerization, charge transfer doping through oxidation-reduction reactions and optical absorption. A straightforward consequence is the appearance of localized states in the band gap between the HOMO and LUMO, as described below.

In conjugated polymers, removing an electron from the HOMO level creates a hole on top of this band (Figure 6(a)). According to the Franck-Condon principle, “electronic transitions are very rapid compared to motions of the nuclei setting up the molecular skeleton [...] Hence, they always take place at constant positions of the nuclei”<sup>22</sup>, which means that the polymeric chain stays in the ground state geometry through the ionization process. As previously said, this geometry is not energetically favorable for an ionized organic molecule, and the chain undergoes a geometry relaxation. This relaxation can be viewed as a redistribution of the  $\pi$ -electrons that polarizes the polymeric chain locally, producing a short range distortion in the array of atoms. The full process results in the

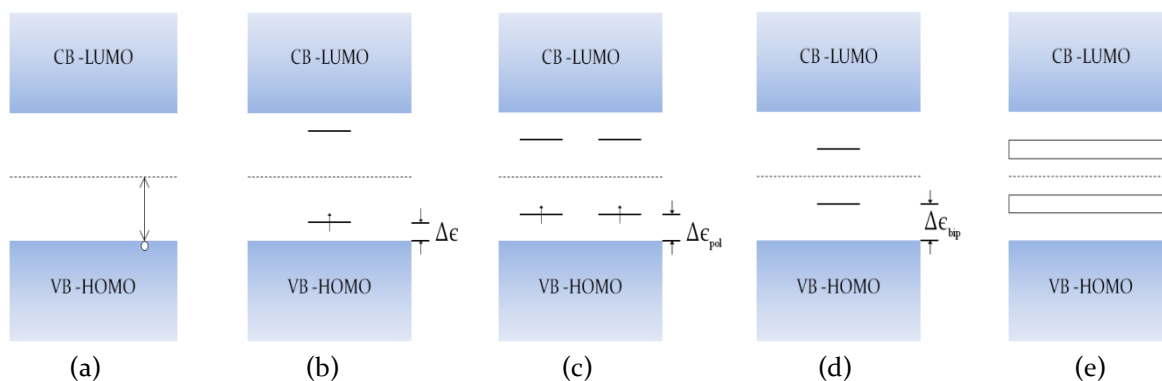


**Figure 6-** Band structure of a conjugated polymer when: (a) Franck-Condon like ionization occurs; (b) a polaron, (c) two polarons, (d) a bipolaron and (e) bipolaron bands are formed. The dotted line represents the Fermi level.

formation of localized electronic states in the band gap due to a local energy shift of the HOMO and LUMO, localizing the electron originally removed (Figure 6(b)). This quasi particle is called a polaron, which in chemical terminology is a  $\frac{1}{2}$  spin radical ion associated with a lattice distortion and localized electronic states in the band gap.

When a second ionization is to be performed on the polymeric chain, two situations are possible: the electron can be removed from any point in the chain, forming a new polaron in the structure (Figure 6(c)); or it can be removed from the existing polaron state, in which case a bipolaron is created (Figure 6(d)). A bipolaron is defined as a spinless quasi particle formed by pair of equal charges associated with the same strong lattice deformation. Since the two charges of equal sign are confined in the same location (the lattice distortion), energy gained during the bipolaron formation process must exceed the Coulomb repulsion between them. Theoretical calculations proved bipolarons are thermodynamically more stable than two individual polarons<sup>23</sup>. Figure 6(c) and (d) show how the electronic states appearing in the band gap for a bipolaron are further away from the valence and conduction band edges than for a polaron, which is expected since lattice relaxation around two charges is stronger than around a single one. Continued ionization of the polymer chain can be performed through, for example, addition of oxidant doping agents. When reaching high dopant concentrations, bipolaron states in the band gap start to overlap between them, leading to the formation of two wide bipolaron bands (Figure 6(e)). These bands enable mobility of bipolarons under the application of an electric field.

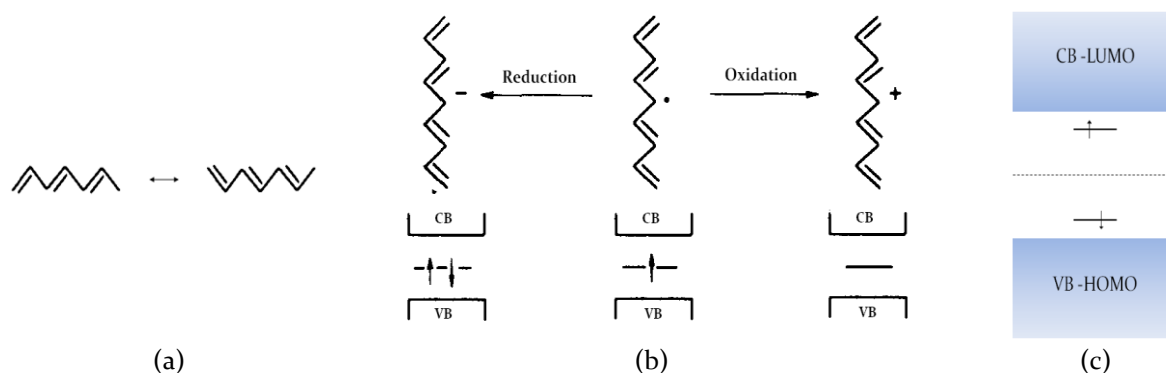


**Figure 7-** (a) Degeneracy of the ground state geometry of trans polyacetylene; (b) schematic illustration of the geometric (top) and band (bottom) structure of a neutral (center), positive (right) and negative (left) soliton on a trans polyacetylene chain (adapted from 23); (c) singlet exciton .

For some conjugated polymers like (*trans*) polyacetylene an interchange of single and double carbon-carbon bonds reproduces exactly the same ground state geometry (Figure 7(a)). It is said these polymers possess *degenerate ground state* systems. When these systems is formed by an odd number of conjugated carbons the unpaired  $\pi$  electron develops into another type of quasi particle called a soliton. A soliton is a localized electronic level at the middle of the band gap with an electron in it (Figure 7 (b)-Center)). A neutral soliton can be oxidized (reduced) in order to create a positive (negative) soliton, as can be seen in the right (left) side of Figure 7(b). Compelled by the degenerate geometry of the system, solitons show their own particular electrical and optical properties in conjugated polymers.

Finally, two polarons of opposite sign can be combined into another type of neutral species, called excitons (Figure 7(c)). This species can be thought of as a coupled electron-hole pair interacting in the same (intra) or different (inter) chains. Light absorption in conjugated polymers always results in the production of these mobile excited states. An exciton remains bounded through Coulomb interactions at a distance that is intermediate between the loosely bound Wannier-Mott excitons and the strongly bound Frenkel excitons (although these limiting type of excitons can also be found sometimes in polymers)<sup>24</sup>. Spin states of the excitons can be singlet or triplet.

## CHAPTER 2

# BASICS OF POLYMER SOLAR CELLS

The conversion of solar radiation into electrical energy is possible thanks to the photovoltaic effect, discovered by French physicist Edmund Becquerel in 1839<sup>25</sup>. When photons are incident upon a material surface, they can be absorbed by the electrons in the valence band, which are excited to higher energy levels and become free to move. Then, a built-in asymmetry in the photovoltaic device prevents these electrons from relaxing to the valence band, driving them instead to external contacts to feed an electrical circuit. Becquerel first noticed the photovoltaic effect while working with silver coated platinum electrodes immersed in electrolyte, observing that an electrical current was created upon illumination. This was the first step in the development of photovoltaic devices. Nevertheless, it wasn't until 1883 that North American inventor Charles Fritts, using the findings from W. Adams and R. Day research<sup>26</sup>, created what is considered the first working solar cell, consisting of a selenium film embedded in two metallic electrodes<sup>27</sup>. The first *p-n* junction silicon solar cell, the most widespread photovoltaic technology up to date, was created in 1953 at Bell Laboratories by Chapin, Fuller and Pearson and converted sunlight with an efficiency of 6%, an outstanding achievement for that time<sup>28</sup>. Commercial silicon solar cells efficiencies nowadays are above 20% (see Figure 2). Other types of inorganic solar

devices such as gallium-arsenide (GaAs), indium phosphide (InP) and cadmium-telluride (CdTe) were successfully developed in subsequent years.

The architectures of polymer solar cells differ from those based on silicon or GaAs due to the major differences in the physical properties of organic and inorganic semiconductors. First and foremost, organic semiconductors have a much lower static dielectric constant than their inorganic counterpart. This comes from the fact that valence electrons in carbon atoms are more tightly bound than those in inorganic semiconductors such as silicon, as can be deduced from their positions in the periodic table. Typical organic semiconductors have dielectric constants of  $\epsilon=3.5-5$ <sup>29,30</sup>, while crystalline silicon of  $\epsilon=11.9$  and GaAs  $\epsilon\approx 13$ <sup>31</sup>. Lower dielectric constants imply larger exciton binding energies, since the attractive Coulomb potential in the electron-hole pair extends over a greater volume, keeping it bounded over larger distances. Exciton binding energies in silicon and GaAs are around 0.015 eV and 0.004 eV<sup>32,33</sup>, respectively, which means thermal energy at room temperature ( $k_B T = 0.025$  eV) is sufficient to dissociate the exciton created by absorption of a photon into an electron and a hole. Hence, light absorption in inorganic semiconductors leads directly to the creation of free charge carriers in standard conditions. Conversely, exciton binding energies in organic semiconductors, ranging from 0.1 eV to 0.5 eV<sup>30</sup>, prevent dissociation of the component charge carriers of the excitons at room temperature. Instead, these mobile excited states remained bounded and then recombine if no external dissociation mechanism is placed. Organic semiconductors are sometimes referred to as excitonic semiconductors for this reason. As separating photogenerated electrons from holes is fundamental for photovoltaics, low dielectric constant in organic semiconductors is a hindrance. To solve this problem, a mechanism of photoinduced electron transfer is implemented (section 2.1).

Another distinctive characteristic of organic semiconductors which is also relevant in the architecture of photovoltaic devices is the low charge carrier mobilities they possess compared to traditional semiconductors. Typically, carrier mobilities in these materials are orders of magnitude lower than in inorganic semiconductors, with values normally ranging from  $10^{-5}$  to  $1$  cm<sup>2</sup>/V·s for both electrons and holes<sup>34,35</sup>. As comparison, silicon presents mobilities around 1400 cm<sup>2</sup>/V·s for electrons and 500 cm<sup>2</sup>/V·s for holes<sup>31</sup>. This difference

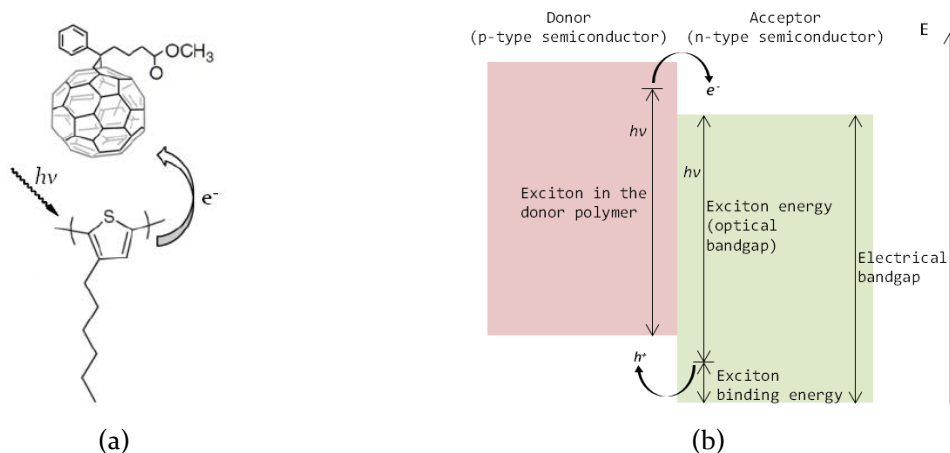


**Figure 8-** (a) Illustration of the photoinduced charge transfer from P3HT to PCBM (adopted from 36); (b) sketch of energy diagram for the process. The band offset between the two materials provides an exothermic way for dissociation of excitons.

affects the design and efficiency of organic solar cells. Nevertheless, lower carrier mobilities in organic semiconductors are partly compensated by their high absorption coefficients  $\alpha$ , usually  $\alpha > 10^5 \text{ cm}^{-1}$ , which means organic layers in photovoltaic devices can be kept thin enough ( $< 100 \text{ nm}$ ) to preserve reasonable charge transport without significantly losing photon absorption.

## 2.1 PHOTOINDUCED ELECTRON TRANSFER

Drawbacks caused by low dielectric constants in organic semiconductors were overcome by the introduction of a photoinduced charge transport mechanism between two materials with different electrical properties<sup>36</sup>. In 1992, two research groups (Morita *et al.*; Sariciftci *et al.*) independently showed that photoinduced electron transfer occurs from an optically excited p-type conducting polymer to a much more electronegative n-type conductive molecule. The notation of donor (D) and acceptor (A) was introduced for these materials, according to their role on the electron transfer mechanism. The process is outlined in Figure 8(a) for the case of the conjugated polymer P3HT and the electron acceptor PCBM<sup>viii</sup>, a fullerene derivate of the spherical C<sub>60</sub> *buckyball*. Figure 8(b) shows the energy diagram of the general process. Upon absorption, the energy of a thermalized exciton (optical band gap) is less than the minimum energy necessary to dissociate it into free

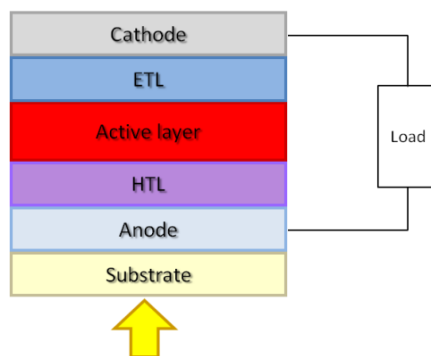
<sup>viii</sup> P3HT = Poly(3-hexylthiophene); PCBM = [6,6]-phenyl-C<sub>61</sub>-butyric acid methyl ester.

charges (electrical band gap) in the p-type semiconductor, due to the effect of the exciton binding energy. However, the thermodynamic requirements for exciton dissociation can be met at the interface with the n-type semiconductor, where abrupt changes of the potential energies (band offset) occur. Since  $E = -\nabla U$ , a local electrical field is formed in this region, acting in opposite directions on each charge carrier of the exciton. When the band offset is greater than the exciton binding energy, as is the case in the band diagram shown, it will be energetically favorable for the excited electron in the donor to be transferred to the acceptor, and the exciton will dissociate. It was demonstrated that the photoinduced electron transfer whole process takes place in the (ultrafast) femtosecond regime<sup>37</sup>, with an efficiency of ~100%.

If the exciton is photogenerated far away from the interface, it may recombine before reaching the interface via intrinsic radiative and non-radiative decay processes. The mean distance  $L_{ex}$  an exciton wanders around before recombining is called *exciton diffusion length*, and is usually 5-30 nm in organic semiconductors<sup>30</sup>, which is considerably less than the optical absorption length  $1/\alpha$ . This limits the thickness of active organic layers in devices and imposes conditions in possible architectures (section 2.8).

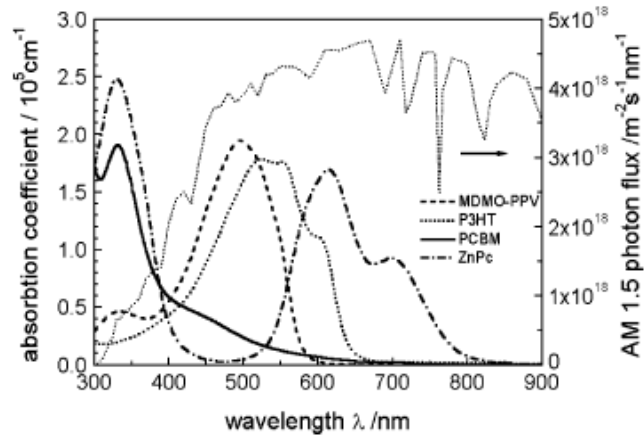
## 2.2 BASIC DESIGN OF A POLYMER SOLAR CELL

Figure 9 shows the basic component layers of a polymer solar cell. No reference to any specific architecture is made. Light enters the device through a transparent substrate, which is usually made of clear glass. Since the photovoltaic effect occurs in the active layer, all layers before that also need to be transparent so the light can reach it. Efforts to exploit the flexibility of polymer semiconductors have led to implementation of flexible substrates, with polyethylene terephthalate (PET) being the most common. The front contact layer or anode is a transparent conductor that works as a hole collector. Although thin films of metallic conductors such as silver, copper or gold have been tried for this layer, their high absorption coefficients are a major setback. Semiconductor oxides, on the other hand, have proven to be a better option for their combination of transparency and high electrical conductivity. Among them, indium thin oxide ( $\text{In}_2\text{O}_3:\text{Sn}$ ), known as ITO, is without doubt, the most widely used transparent conductor not only in photovoltaics but in other



**Figure 9-** Basic design of a polymer solar cell. Light enters the device through a transparent substrate and is absorbed in the active layer, which imposes the requirement of transparency on the anode and hole transporting layer (HTL). The HTL, along with the electron transporting layer (ETL), improve the overall performances of organic solar cells, enhancing charge transport throughout the device. Nevertheless, their use is optional. The anode and cathode collect the photogenerated charges and introduce them to an external circuit.

applications such as light emitting diodes (LEDS) or electrochromic devices. Next is the hole transporting layer (HTL), which is used as a transparent conducting material to improve the transport and collection of holes generated during the exciton dissociation process inside the active layer. The most commonly used HTL consist of the semiconducting polymer mixture poly(3,4-ethylenedioxythiophene)-poly(styrenesulfonate) or PEDOT:PSS, due to its high hole conductivity and good transparency. Over the HTL the active layer is placed. As said before, the active layer is where the photovoltaic effect takes place in the solar cell. First, the active layer absorbs an incident photon and then makes use of the photoinduced electron transfer mechanism to dissociate the photogenerated exciton into a free electron hole pair. A variety of organic materials and architectures are available, and the choice depends on the type of device and experiment to be made. Finally, the electron transporting layer (ETL) and the rear contact are in charge, respectively, of the transport and collection of the electrons resultant from the exciton dissociation in the active layer. Normally, these layers consist of metallic films of different work functions, being the most common ones calcium and aluminum. A thorough description of the fabrication process, deposition techniques as well as details of the materials implemented is made in the experimental section. Is important to note that the use of the HTL and ETL is optional, as, technically, the photovoltaic process can occur without them being present in the solar cell. Their use is solely to take advantage of their enhanced charge carrier transport properties that facilitate the collection in the devices, improving the performances of organic solar devices.



**Figure 10-** Absorption coefficients of a few organic materials commonly used in the active layers of photovoltaic cells. For comparison, standard AM 1.5 terrestrial solar spectrum is included (Adopted from 36).

### 2.3 WORKING PRINCIPLES

The process of light conversion into electric current in organic solar cells is divided in five consecutive steps that can be studied independently: (i) photon absorption in the photoactive layer of the device, leading to the formation of an exciton; (ii) diffusion of the exciton to the interfacial region; (iii) exciton dissociation; (iv) charge transport to the anode (holes) and cathode (electrons); and finally (v) charge collection at the metallic contacts.

For efficient light collection, the absorption spectrum of the photoactive layer should match the solar emission spectrum. A band gap of 1.1 eV, such as in silicon,<sup>31</sup> is capable of absorbing almost 80% of sunlight on the earth's surface.<sup>36</sup> However, rather large band gaps in semiconducting polymers ( $\geq 2$  eV) limit the portion of incident sunlight that can be absorbed to the blue side of the solar spectrum ( $\leq \sim 620$  nm), which accounts approximately for 30% of solar irradiation on earth.<sup>36</sup> Figure 10 displays the absorption coefficients of some organic materials commonly used in active layers, in comparison with the AM 1.5 standard solar spectrum.<sup>ix</sup> In spite of high absorption coefficient values, materials with better spectral absorption of sunlight photons are needed.

As previously described, the absorption of a photon in the active layer produces a photogenerated exciton that diffuses to the interfacial area between the donor and the

<sup>ix</sup> A description of solar spectrum conventions for testing of solar cells is included in section 3.4.4.

acceptor material for dissociation. The absorption must occur a distance  $d$  away from the interface such that  $d \leq L_{ex}$ , otherwise the exciton recombines and its energy is lost. This requires that the donor-acceptor phase length should be of the same order of magnitude as  $L_{ex}$ . The fraction of absorbed photons depends on the absorption spectrum (absorption coefficient) of the materials, the thickness of the layers and possible internal reflections of the light. The percentage of dissociated excitons depends mainly on  $L_{ex}$ , the thickness of the layers, charge mobility of the materials and the charge separation probability in the interfacial region.

Once the exciton is dissociated and the charge carriers become free from the interface, they can contribute to the photocurrent by traversing the films in the active and charge transporting layers and being collected at the electrodes. However, they can recombine in a second order process if they return to the interfacial region in the active layer. To avoid this and to promote charge collection, a net force for driving free charge carriers to the electrodes must be established. There are only two important forces that can drive the charge carriers throughout the solar cell: internal electric fields set by potential gradients  $\nabla U$ , and charge carrier concentration gradients  $\nabla \mu$ . Together, they make up the gradient of the quasi Fermi level  $\nabla E_f$  of the charge carriers within the device. Internal electric fields lead to a *drift* current, while the charge carrier concentration gradients induce *diffusion* currents. The general expression for the 1-D electron current density through a device is<sup>28</sup>:

$$J_n(x) = n(x)\mu_n \nabla U(x) + k_B T \mu_n \nabla n(x) \quad (2.1)$$

where  $n(x)$  is the electron concentration,  $\mu_n$  is the electron mobility,  $k$  is the Boltzmann constant and  $T$  is the absolute temperature. An analogous equation describes the hole current density. Equation (2.1) does not make any references to specific devices. The only assumption made is that besides the electrical and particle concentration potentials, no other potential gradients (such as temperature, pressure, magnetic, etc.) affect the electron current density. Equation (2.1) is valid both for a device in the dark and under illumination, as well as in equilibrium and away from it.

The expression for the thermodynamic equilibrium is <sup>29</sup>:

$$\mu = k_B T \ln[n(x)] + \text{const.} \quad (2.2)$$

taking the gradient:

$$\nabla\mu(x) = \frac{k_B T}{n(x)} \nabla n(x) \quad (2.3)$$

and substituting (2.3) in (2.1):

$$J_n(x) = n(x)\mu_n [\nabla U(x) + \nabla\mu(x)] \quad (2.4)$$

which shows that  $\nabla U$  and  $\nabla\mu$  correspond to equivalent forces for the electron current. The same can be concluded for holes. The relative importance of  $\nabla U$  and  $\nabla\mu$  in a device is considerably different between organic and inorganic solar cells. Because photogeneration processes occur in the bulk of inorganic devices, and due to their high carrier mobilities (which minimize concentration gradients)  $\nabla\mu$  plays an almost insignificant role in inorganic photovoltaics. They are majorly driven by electric field induced currents. Conversely, since photogeneration process at interfacial regions increases the carrier concentration gradients,  $\nabla\mu$  plays a preponderant role in net current of organic cells. Diffusion currents complement the effects of drift currents in these devices, and even surpass them in certain occasions. The most extreme example of this behavior is the case of organic dye-sensitized solar cells, which are based entirely on  $\nabla\mu$ , with  $\nabla U \approx 0$ .

Once the charge carriers reach the edges of active and transport layers, they are extracted from the device by two selective (metallic) contacts. This selectivity is achieved through their work functions of the electrode materials. Details about the metal/semiconductor interface are given in section 2.7. The final efficiency of the solar cell is a product of efficiencies for each of the steps involved in the photocurrent production:

$$\eta = \eta_a \times \eta_{diff} \times \eta_{dis} \times \eta_{tr} \times \eta_{cc} \quad (2.5)$$

where: *abs* = photon absorption, *diff* = exciton diffusion, *dis* = exciton dissociation, *ct* = charge transport, *cc* = charge collection.

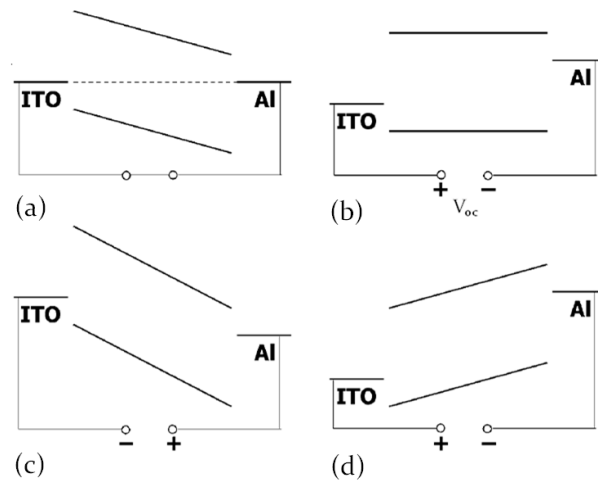


**Figure 11-** Depiction of the MIM model applied to a photovoltaic cell in different regimes: (a) short circuit condition: photogenerated charge carriers drift towards the electrodes under illumination; (b) open circuit condition: no current flow, (c) reverse bias: photogenerated charges drift in strong electric fields; (d) forward bias larger than  $V_{oc}$ : injected charge current flows. The HOMO and LUMO bands of the semiconductor, as well as the Fermi levels of the metals, are indicated. (Adopted from [38])

#### 2.4 THE METAL-INSULATOR-METAL MODEL

As described in the previous section, electric potential gradients in solar cells are an important force driving free charge carriers to the metallic contacts. A common form to establish electric gradients in these devices is employing electrodes with different work functions. This method is well described in the Metal-Insulator-Metal (MIM) model, one of the simplest representations for thin organic solar cells (among other devices). Figure 11 presents a general depiction of this model. An organic semiconductor is sandwiched between two metals with different work functions. The HOMO and LUMO bands of the semiconductor are presented, as well as the Fermi levels of the metals. The system can be in different *working regimes* due to externally applied voltages. In Figure 11(a) the two electrodes are in short circuit conditions and no external voltage is applied. A built-in electric field evenly distributed throughout the device results from the difference in the metals' work functions: electrons diffuse from highest to lowest Fermi level electrode until equilibrium is reached, creating an electric potential difference that bends the energy levels in the semiconductor. When the device is in the dark, no net current flows through the circuit. Under illumination conditions, free charges can drift towards the contacts thanks to the built-in electric field; electrons move towards the lower work function electrode and

holes to the opposite one. A *short circuit current*  $J_{sc}$  flows through the circuit and the solar cell works. A forward bias, defined with the positive terminal in the lowest work function metal, can be applied to compensate the built-in electric field and the *flat band condition* is obtained (Figure 11(b)). This voltage corresponds to the difference in the metals' work functions and is called *open circuit voltage*  $V_{oc}$ , since this is the voltage that can be accumulated in the cell when illuminated in open circuit conditions<sup>x</sup>. The net current is zero in this case. Applying a reverse bias increases electric gradient in the device, as shown in 11(c). A very low current flows for a cell in the dark under these conditions. Under illumination, charge carriers are driven by the strong electric field for the cell in this case. This effect is used in photodetector devices. Finally, a forward bias can inject charge carriers into the semiconductor if it is larger than  $V_{oc}$  (11(d)). If these charges are able to recombine, the device can work as a light emitting diode (LED). It is important to note that results from this model are more precise for un-doped semiconductors.

## 2.5 CURRENT-VOLTAGE CHARACTERISTICS

The MIM model can help understanding the rectifying behavior present in current-voltage curves ( $I \times V$  or  $J \times V$ )<sup>xi</sup> of solar cells. Figure 12 shows the  $J \times V$  characteristics of a typical solar cell both in the dark and under illumination conditions. Without light, these devices have the same electrical characteristics of a diode: no current flow exists around the short circuit regime, but as a forward bias is applied and charge carriers are injected it starts to increase. Once the bias exceeds the open circuit voltage, this *injected current* grows exponentially. When the cell is illuminated a photocurrent  $J_{ph}$  opposed to the injected current is generated. Opposite directions of injected and photogenerated currents are expected since the forward bias and the built-in potential have opposite directions as well (Figure 11(a) and (d)). The photocurrent maximum is found in the short circuit conditions ( $J_{sc}$ ), and it decreases as charge injection by forward bias is performed. As seen in Figure 12, the light has the effect of shifting the  $J \times V$  curve down into the fourth quadrant, where power  $P_{out} = I \times V$  can be extracted from the solar cell. Therefore, its operating range is  $0 < V < V_{oc}$ .

<sup>x</sup> Further comments on the  $V_{oc}$  of bilayer and bulk heterojunction solar cells is made in section 2.8.

<sup>xi</sup> Although  $J$  clearly refers to *current densities*, the shorthand *current* is occasionally used in this text for simplicity reasons.

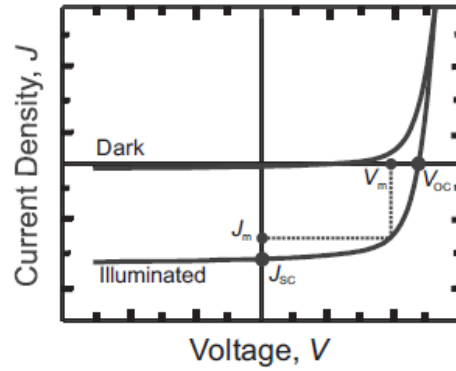


**Figure 12-** Typical *Current–Voltage* characteristics of a solar cell in the dark and under illumination. The short circuit current  $J_{sc}$  and open circuit voltage  $V_{oc}$  are indicated. Maximum power output of the cells is at the point  $(V_m, J_m)$ , denoted by the dotted rectangle (adopted from 34).

The greater the light intensity the larger the downward shift and the power generated. The maximum power output delivered by the cell is given by the product  $J_m \times V_m$ , indicated with a dotted rectangle in Figure 12. The highest photocurrent  $J_{sc}$  and highest voltage  $V_{oc}$  in the device operating range denote another rectangle use for the characterization, as the ratio

$$FF = \frac{J_m V_m}{J_{sc} V_{oc}} \quad (2.6)$$

called *Field Factor (FF)*, defines the “squareness” of the  $J \times V$  curve; the part of the  $J_{sc}$ - $V_{oc}$  rectangle that can be actually used. This parameter indicates the quality of the diode. Optimized solar cells show  $FF$  in the range of 0.5-0.7<sup>39</sup>. Higher  $FF$  cells deliver more power. Although equation (2.6) gives the maximum theoretical  $FF$  value, in practice it might be lower due to the presence of parasitic resistive losses (next section). The photovoltaic power conversion efficiency (PCE) of a solar cell is defined as the ratio of the maximum power  $P_m$  delivered by the device to the incident total power of electromagnetic radiation  $P_{in}$ :

$$\eta = \frac{P_m}{P_{in}} = \frac{J_m V_m}{P_{in}} = \frac{J_{sc} V_{oc} FF}{P_{in}} \quad (2.7)$$

where equation (2.6) was introduced in the last step. Large  $FF$ ,  $J_{sc}$  and  $V_{oc}$  are required for high efficiencies. Generally, PCE is the most important parameter for evaluation of a photovoltaic device, as it summarizes all mechanism involved in the photovoltaic process. Record organic solar cells efficiencies were shown in Figure 2, although common experimental values in the literature can be much lower.

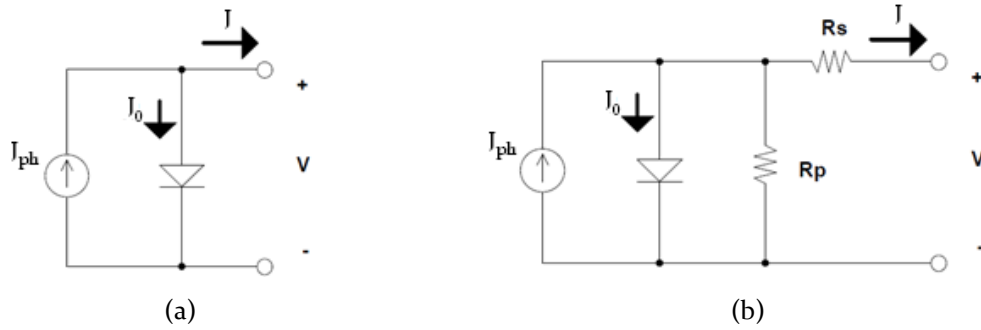


**Figure 13-** Equivalent circuit of an (a) ideal and (b) real organic solar cells showing the total current  $J$ , the photogenerated current  $J_{ph}$  and the diode dark saturation current  $J_0$ . The latter also shows the series and parallel resistances,  $R_s$  and  $R_p$ . Other resistors, capacitors and diodes can be added to model more complex behaviors.

## 2.6 IDEAL VS. REAL PHOTOVOLTAIC CELLS

Another important approximation often used to model the current-voltage characteristics of solar cells is the equivalent circuit representation. Important charge transport properties of the device can be analyzed in this model to help understand experimental results.

An *ideal* solar cell is characterized by two main features: (i) no electrical resistance for charge carriers flowing towards the electrodes, (ii) no leakage of photogenerated current. The equivalent circuit of an ideal solar cell is shown in Figure 13(a). The total current in such a cell is given by the diode (injected) current  $J_D$  minus the photogenerated current  $J_{ph}$ :

$$J = J_D - J_{ph} \quad (2.8)$$

$$J = J_0 \left( e^{\frac{eV}{k_B T}} - 1 \right) - J_{ph} \quad (2.9)$$

where the ideal diode equation<sup>28</sup> was inserted in (2.9);  $J_0$  is the diode saturation current,  $e$  is the elementary charge,  $V$  is the applied external voltage,  $k_b$  is Boltzmann constant and  $T$  is the absolute temperature. The minus signal in  $J_{ph}$  comes from the fact that the photocurrent opposes the injected current  $J_D$ . The  $JxV$  characteristics of an ideal solar cell shows a  $FF \approx 1$ , which means basically all of the power in the  $J_{sc}$ - $V_{oc}$  rectangle can be delivered by the device. By definition, it is the most squared a  $JxV$  curve can be (dashed/dotted line in Figure 14).

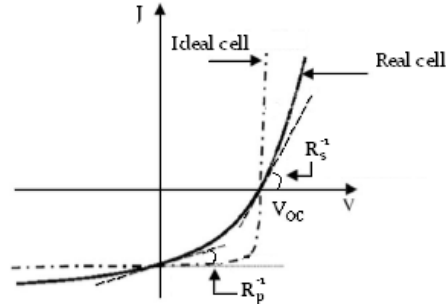


**Figure 14-**  $JxV$  characteristics for an ideal and real solar cell. Ideal cell's curve possesses a much higher field factor than the real cell, as can be deduced from the "squareness" of the curves.

As usual, ideal devices exist only in the theoretical descriptions and no such a thing as an ideal solar cell can be experimentally fabricated. *Real* photovoltaic cells exhibit resistance to charge carrier transport and leaking of photogenerated currents. In consequence, a more realistic equivalent circuit is needed to model the electrical behavior of photovoltaic devices accurately. Figure 13(b) shows an equivalent circuit of a solar device including the parameters  $R_p$  and  $R_s$ , known as the parallel and series resistances, respectively. These parameters take into account possible experimental deviations from the ideal behavior.  $R_s$  represents the sum of the resistances from the bulk of the materials and interfaces between them, including the electrodes.  $R_p$  is the resistance leakage currents experience in their way off collection at the electrodes. A good photovoltaic performance requires  $R_p \gg R_s$ . High values of  $R_s$  could come from low carrier mobilities and charge extraction barriers at interfaces, while low  $R_p$  may result from poor thermal evaporation process of the metallic electrode, creating conduction paths outside the cell's circuit. The generalized Shockley equation<sup>28</sup> describes the current of the real cell's equivalent circuit:

$$J = \frac{R_p}{R_s + R_p} \left[ J_0 \left( e^{\frac{e(V-JR_s)}{nk_bT}} - 1 \right) + \frac{V}{R_p} \right] - J_{ph} \quad (2.10)$$

where  $n$  is a parameter called the *diode quality factor*, a number between 1 and 2 that also describes deviations from the ideal cells ( $n=1$ ),  $J_0$  is the diode dark saturation current. When  $R_s = 0$  and  $R_p \rightarrow \infty$  equation (2.10) correctly reduces to the ideal case equation (2.9). High values of  $R_s$  reduce the short circuit current  $J_{sc}$ , while low  $R_p$  reduce the open circuit voltage  $V_{oc}$ . Both cases have a negative impact on the  $FF$  values as well, as can be seen on the poor  $JxV$  behavior of the real solar cell in Figure 14. Fair estimations of  $R_s$  and  $R_p$  can be obtained from the reciprocal of the slope of  $JxV$  near the  $V_{oc}$  and  $J_{sc}$  points, respectively (Figure 14).

## 2.7 METAL-SEMICONDUCTOR JUNCTION

Although useful to describe the internal electric field within the bulk of a solar cell, the MIM model fails to describe the electrical behavior observed at interfaces between metals and doped semiconductors. Since a great amount of organic semiconductors used in solar cells are doped, and since transport properties at this interface are of extreme importance in the photocurrent collection process, understanding the physical phenomena taking place in this region is important for the analysis of experimental results. This is done with the aid of the metal-semiconductor (M/S) junction picture.

When a metal comes in contact with a doped semiconductor material, either a rectifying or non-rectifying contact is obtained. The former is known as a Schottky junction, after German physicist Walter H. Schottky, who first<sup>xii</sup> explained its behavior in 1938<sup>39</sup>. The latter is an ohmic contact. Whether a given M/S junction forms a Schottky or ohmic junction depends on two factors: (i) the relative values of the metal and semiconductor work functions, and (ii) the type of doping ( $n$  or  $p$ ) performed on the semiconductor.

The case is presented for an  $n$ -type semiconductor in Figure 15. In (a) and (b) the work function  $\phi_M$  of the metal is higher than that,  $\phi_S$ , of the semiconductor, forming a Schottky-like junction when brought together. In (c) and (d) the work functions are such that  $\phi_M < \phi_S$ , and the M/S junction forms a non-rectifying ohmic contact. The Schottky junction exhibits an electric potential barrier for the carriers in charge of current transport (Figure 15(b)); the electrons in the conduction band  $E_c$  of the  $n$ -type semiconductor have to overcome a potential barrier of height  $\phi_{BS}$  as they drift from the semiconductor to the metal, and a barrier  $\phi_B$  in the opposite direction. This barrier, called Schottky barrier, results from alignment of the (initially different) Fermi levels of the metal  $E_{FM}$  and semiconductor  $E_{FS}$  when put in intimate contact. Charge carriers flow from the semiconductor to the metal until Fermi levels are equilibrated. This flow leaves behind uncompensated  $N_D^+$  donors in a region of depth  $w$  inside the semiconductor, known as *depletion region*, which creates an electrostatic potential gradient that bends the valence ( $E_v$ ) and conduction ( $E_c$ ) bands.

---

<sup>xii</sup> Schottky published a short overview in advance to ensure priority over Nevill F. Mott, who independently explained the rectifying behavior of the M/S junction that year.

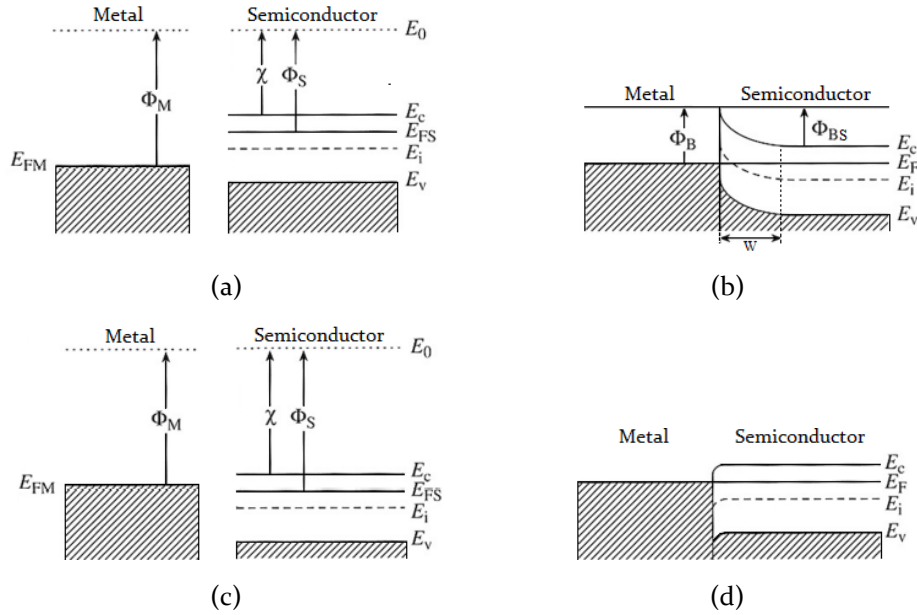


**Figure 15-** M/S junction formation for an  $n$ -type semiconductor. Metal's:  $\Phi_M$  = work function,  $E_{FM}$  = Fermi level; Semiconductor's:  $\chi$  = electron affinity,  $\phi_S$  = work function,  $E_c$  = conduction band,  $E_v$  = valence band,  $E_{FS}$  = Fermi level,  $E_i$  = intrinsic Fermi level;  $E_o$  = vacuum level,  $E_F$  = equilibrium Fermi level,  $\phi_B$  = potential barrier blocking electron flow from M to S,  $\phi_{BS}$  = potential barrier from S to M,  $w$  = depletion region depth. A Schottky barrier (b) is formed when  $\Phi_M > \Phi_S$  (a); an ohmic contact (d) is formed when  $\Phi_M < \Phi_S$  (c).

An inspection of Figure 15(a) and (b) shows that heights of the potential barriers are:

$$\Phi_B = \Phi_S - \chi \quad (2.11)$$

$$\Phi_{BS} = \Phi_M - \Phi_S \quad (2.12)$$

with  $\chi$ =semiconductor's electron affinity. These parameters define the charge carrier current through the junction. When a forward bias  $V$  (positive terminal on the metal) is applied, the Schottky barrier  $\phi_{BS}$  is reduced and electron current flow at the interface is unbalanced, resulting in a large net *forward current* (from S to M). The current increases exponentially with  $V$ . On the other hand, a reverse bias will increase  $\phi_{BS}$ , resulting in small net *reverse current* (from M to S). This explains the rectifying behavior of the Schottky junction.

The M/S junction forms a non-rectifying ohmic contact when  $\Phi_M < \Phi_S$ , as in 15(c). Alignment of Fermi levels also causes the bending of conduction  $E_c$  and valence  $E_v$  bands of the semiconductor, with the difference that this time instead of an electrostatic potential

Work functions relationship	<i>n</i> -type semiconductor	<i>p</i> -type semiconductor
$\Phi_M < \Phi_S$	Ohmic	Schottky
$\Phi_M > \Phi_S$	Schottky	Ohmic

**Table 1-** Generalization of the M/S work function relationships for the appearance of Schottky and ohmic contacts, for both *n* and *p* type semiconductors.

barrier a continuous conducting band is created at the interface (Figure 15(d)). In the ideal case, an ohmic contact allows electron transport between materials with no resistance at all. When a bias  $V$  is applied in either direction, a large amount of current flows through the contact, which means no rectification behavior exists.

A similar analysis can be made for a *p*-type semiconductor in a M/S junction. Rectifying Schottky and ohmic contacts will emerge in opposite conditions compared to those of *n*-type semiconductors in M/S junctions, i.e., a Schottky junction will appear when  $\Phi_M < \Phi_S$ , while ohmic contacts in the reverse situation. Table 1 summarized these conditions. Barrier heights for the Metal/*p*-type semiconductor will be given by:

$$\Phi_B = IP - \Phi_M \quad (2.13)$$

$$\Phi_{BS} = \Phi_S - \Phi_M \quad (2.14)$$

where IP is the ionization potential of the semiconductor (energy difference between the HOMO and vacuum levels).

## 2.8 DEVICE ARCHITECTURES

As described in the beginning of this chapter, design of organic solar cells is governed by the unique properties of organic semiconductors. Low dielectric constants, high exciton binding energies, low carrier mobilities, high absorption coefficients (especially in the most energetic part of the spectrum), as well as the charge carrier driving forces are part of the features to be taken into account in the designing of the architectures of polymer solar cells. A brief description of the most common architectures is presented.

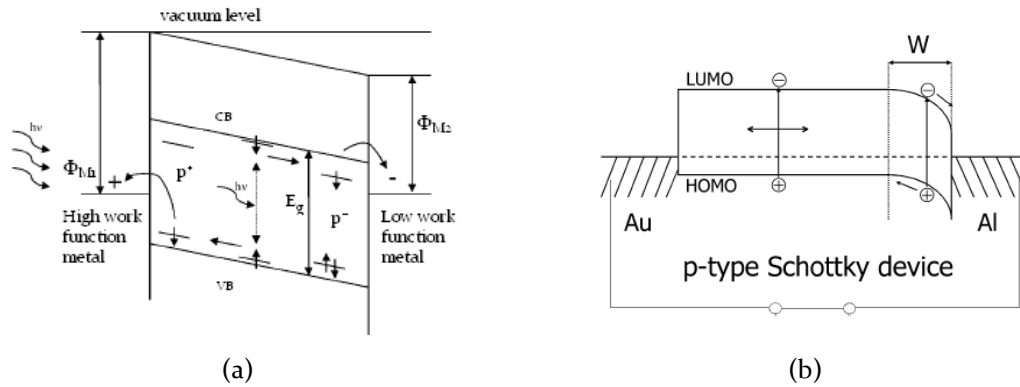


**Figure 16-** Monolayer cell viewed under the: (a) MIM model, under short circuit conditions; (b) Schottky junction picture, where a Schottky barrier forms at the aluminum electrode and an ohmic contact at the Au. VB = valence band, CB = conduction band,  $E_g$  = bandgap,  $P^+$  and  $P^-$  = positive and negative polarons. (Adopted from 40 and 38, respectively)

### 2.8.1 SINGLE LAYER

The first polymer solar cells were based on a single layer of semiconducting polymer sandwiched between two metal layers of different work functions<sup>40</sup>. Figure 16(a) shows a diagram of these early devices using the MIM model. An important limitation in these cells was that electrostatic potential due to the work functions difference wasn't high enough for efficient photogenerated charge generation. Another approach employed a Schottky junction between the semiconducting polymer and one of the electrodes<sup>40</sup> (Figure 9(b)). In this case, the depletion region  $w$  provides an electric field in which excitons can be dissociated. However, only the small portion of them generated at a distance  $d \leq L_{ex}$ , the exciton diffusion length, from  $w$  are separated into free charges. Therefore, the problem of photoinduced charge generation was not overcome by this method.

### 2.8.2 BILAYER HETEROJUNCTION

A major breakthrough was achieved in 1986 by C. W. Tang<sup>41</sup>, who introduced the concept of a bilayer structure sandwiched between two dissimilar electrodes. An organic *heterojunction*, a system of two organic semiconductors with different bandgaps and carrier transport properties, was placed between metals with different work functions. Tang

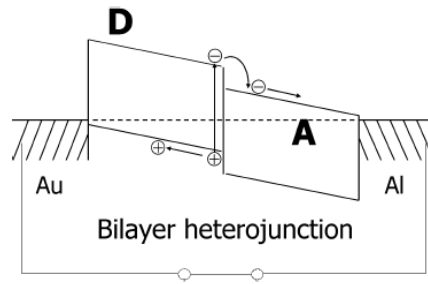


**Figure 17-** Depiction of a planar bilayer heterojunction. Photogenerated exciton can only be dissociated in a thin layer at the heterojunction interface. (Adopted from 38)

reported a power conversion efficiency of around 1%, an outstanding result for the time, which remained a benchmark for many years. The bilayer architecture consists of two semiconducting polymers, one acting as electron donor (D) and the other as acceptor (A), stacked together in a planar interface where the exciton dissociation occurs (Figure 17).

After separation, free electrons travel in the acceptor semiconductor towards the Al electrode, independently of the holes which remain traveling in the donor towards the Au. A great portion of exciton recombination is prevented with this charge transport mechanism. Figure 17 depicts the energy levels in these bilayer devices, neglecting possible band bending. The difference in the ionization potential of the donor and the electron affinity of the acceptor provides the electric potential gradient for charge separation.

Photogenerated excitons must reach the D/A interface before they recombine. Only excitons generated within a diffusion length  $L_{ex}$  to the interface can contribute to the photocurrent, which limits the thickness of the heterojunction. This undermines absorption of the devices, ultimately reducing its efficiency.

### 2.8.3 Bulk heterojunction

The limitation of thin organic layers was finally overcome with the invention of the bulk heterojunction (BHJ) architecture; a concept based on the ultrafast electron transfer mechanism (section 2.1). First introduced by G. Yu and coworkers in 1995<sup>42</sup>, the BHJ consists of an interpenetrating network of donor and acceptor materials blended at the nanometric scale. Consequently, continuous D/A interfaces are formed throughout the bulk of the active

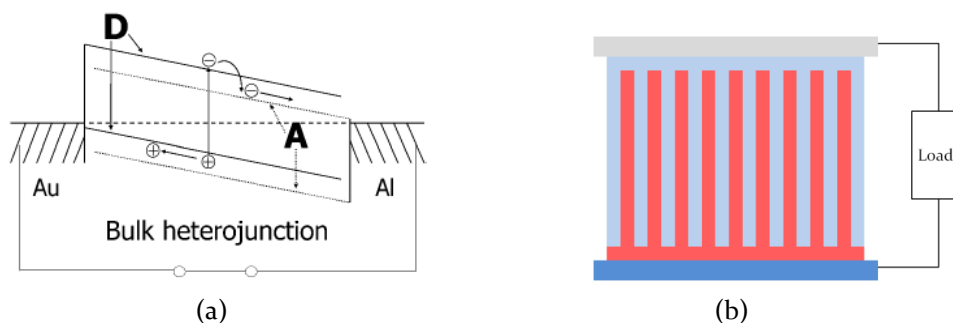


**Figure 18-** Bulk heterojunction solar cell: (a) energy levels diagram (Adopted from 38); (b) ideal architecture design of the active layer. Photogenerated exciton can be dissociated throughout the whole active layer.

layer and the distance  $d$  excitons travel to reach it is significantly reduced. In optimized solar cells  $d < L_{ex}$  (exciton diffusion length), which is the case of fullerene-based solar cells<sup>36</sup>. Figure 18(a) depicts the energy diagram of a bulk heterojunction solar cell. Excitons can be photogenerated anywhere inside the active layer and still find its way to dissociation in the D/A interface extended throughout the bulk.

However, BHJ architecture presents a new challenge. Photogenerated charges carriers must be able to reach the collecting electrodes through this intimately blended network, but random distribution of component materials can lead to charge traps at bottlenecks or dead ends in the charge conduction pathway. Since electrons and holes are independently transported in the acceptor and donor semiconductors, respectively, these materials should be ideally mixed into a *ordered* bulk heterojunction, as in Figure 18(b), that avoids such charge traps. Research in this area is still ongoing<sup>43</sup>.

Finally, is important to review the definition of open voltage  $V_{oc}$  given in section 2.4. Back then it was said that  $V_{oc}$  equals the difference in the work functions of the electrodes implemented. Although it fits the simple description of the  $JxV$  curves in the MIM model, which can be used (with limitations) for modeling single layer devices; this definition tends to decouple from experimental results as architectures of solar cells get more complicated. Nanoscale morphology, charge carrier recombination and carrier losses at the electrodes are some of the factors that affect the  $V_{oc}$ . More accurate calculations of  $V_{oc}$  in organic solar cells indicate it is linearly dependent on the HOMO and LUMO levels of the donor and acceptor,

respectively <sup>36</sup>. For the specific case of fullerene-based BHJ devices, this parameter can be calculated by <sup>44</sup>:

$$V_{oc} = \frac{1}{e} (|HOMO_{Donor}| - |LUMO_{Acceptor}| - \Delta) - \frac{k_B T}{e} \ln \left( \frac{n_e n_h}{N_c^2} \right) \quad (2.15)$$

where  $N_c$  = density of states at the fullerene LUMO, defined identically for the density of states at the polymer HOMO,  $n_e$  = electron density,  $n_h$  = hole density at open circuit,  $\Delta$  = energy shift from disorder within the heterojunction and/or separated polymer-fullerene regions. The second term, which has been estimated to be 0.3 eV, takes into account shifting of the quasi Fermi levels into the gap due to temperature effects <sup>44</sup>.

## CHAPTER 3

# EXPERIMENTAL DETAILS

### 3.1 MATERIALS

Photovoltaic devices studied in this work consists of bulk heterojunction polymer solar cells with commercial P<sub>3</sub>HT:PCBM donor/acceptor blend as the active layer (Plexcore PV Photovoltaic Ink by Aldrich<sup>®</sup>) on a PEDOT:PSS blend (Bayrton<sup>®</sup>), used as a hole transporting layer. They both are spin coated over commercial Indium Tin Oxide (ITO) coated glass (Delta Technologies<sup>®</sup>), which is the most common transparent electrode used for this type of cells. As the rear contact, a Calcium/Aluminum bilayer is deposited over the active layer by thermal evaporation.

The photovoltaic ink used for the active layer was chosen due to its high absorption in the visible range (see Figure 10), high molecular weight and highly regioregular grade of P<sub>3</sub>HT, which produces highly organized films. This accounts for an improve performance of photovoltaic devices. Furthermore, since there is no need for in-house formulation or synthesis, performance deviations related to material variability in the active layer are minimized and regular behavior of the active layer allows focusing on studies in other areas.

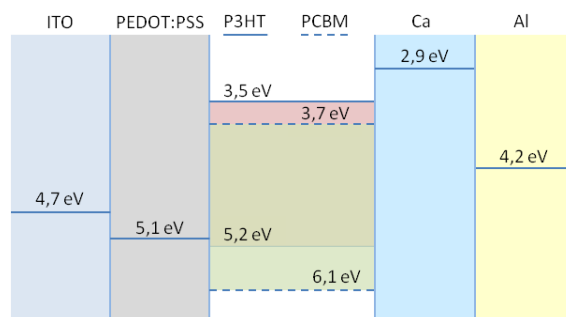


**Figure 19-** Energy level diagram of the bulk heterojunction solar cells fabricated in this work.

The Baytron<sup>®</sup> PEDOT:PSS blend is a 1.3 wt % water solution conductor with conductivity of about  $1 \text{ S}\cdot\text{cm}^{-1}$ . Its work function,  $\sim 5.1 \text{ eV}$ , lies between the work function of ITO and the HOMO of P<sub>3</sub>HT polymer (Figure 19), enhancing the charge carrier collection on the ITO anode due to energy barrier reduction for holes transportation (section 2.7).

With a band gap greater than 3 eV ITO shows great transparency ( $>80\%$ ) in the visible region, which, along with a high electrical conductivity make it the most used and widely studied transparent conductor among the oxides<sup>45,46</sup>. It is used not only for photovoltaic devices, but also for LCD screens, LEDs, photodetectors, etc. ITO coated glass from Delta Technologies<sup>®</sup> consists of a layer of about 100 nm thick, with a mean roughness of 4 nm. It has an electrical resistance of 8-10  $\Omega/\text{sq}$  and a work function value of about 4.7 eV. This work function makes a good match with that of the PEDOT:PSS layer.

The cathode consists of the thermal evaporated metallic bilayer Ca (30 nm)/Al (70 nm), materials that were specifically selected mainly for two reasons: (i) their work function improves photogenerated electron collection in the PCBM through ohmic contacts, while blocking holes in the P<sub>3</sub>HT due to potential barrier formation; (ii) this bilayer eliminates the charge accumulation that occurs when an Al monolayer is used instead. Furthermore, Al is deposited on top of Ca as a protection layer due to the poor stability of Ca in air.

Figure 19 shows the energy band diagram of the materials used in the fabrication of bulk heterojunction solar cells of this work. Note that, when ITO interfaces PEDOT:PSS, the energy barrier between the anode and the P<sub>3</sub>HT is reduced, improving hole collection (see section 2.7).

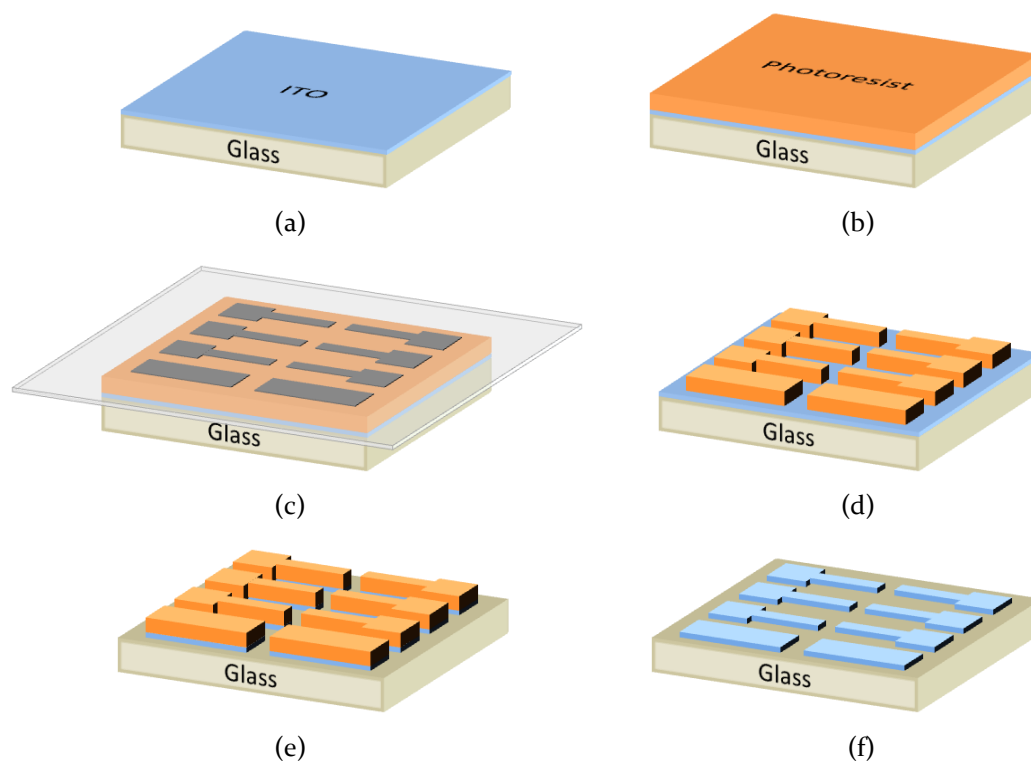


**Figure 20-** Photolithography procedure performed on the ITO/glass substrate; (a) ITO/glass substrate before photolithography, (b) spin casted photoresist on ITO, (c) UV exposition of photoresist through a mask, (d) developed photoresist pattern, (e) etched ITO layer still with photoresist, (f) ITO electrodes array on glass, consisting of two ground contacts (rectangles) and six electrodes for solar cells.

### 3.2 ITO PHOTOLITHOGRAPHY AND SUBSTRATE PREPARATION

The commercially obtained ITO coated glass was cut in  $\sim 20.5$  mm x 10.5 mm slides. As mentioned, it consists of a  $\sim 100$  nm ITO layer over the glass surface (Figure 20 (a)). For an accurate delimitation of the actual effective area of each solar cell, as well as to avoid short circuit problems, an array of electrodes needs to be pattern on the ITO layer by etching some of it from the glass substrate. For this, a photolithography procedure is performed on the ITO layer prior to casting of organic layers.

This procedure is depicted in Figure 20. Positive photoresist was spin-coated on the ITO-coated glass slides at 300 rpm for 20 s (Figure 20(b)). Then, it was soft-baked at  $90^{\circ}\text{C}$  for 120 s and exposed to UV light through a mask for 120 s (Figure 20(c)). The photoresist patterns were then developed in developer solution for 60 s and briefly washed with

deionized (DI) water (20(d)). ITO substrates with patterned photoresist layer were then immersed in an etching solution consisting of HCl (8M) for about 15 min. The pattern now appears on the ITO layer (20(e)). The conductivity of etched areas was measured to verify the removal of ITO. The remaining photoresist was removed by placing it into deionized water, acetone and isopropyl alcohol for 1 minute each. The final array patterned on each ITO slide (20(f)) consists of two ground contacts (rectangles) and six electrodes for solar cells.

Next, the photolithographed ITO substrates were cleaned. This is a critical step, since the ITO surface will interface the PEDOT:PSS and any impurities on the ITO can change physical and chemical properties of this interface and the overall performance of the devices. The cleaning process consists in ultrasonic bath in the following solutions: detergent (Extran<sup>®</sup>), acetone and isopropyl alcohol; for fifteen minutes each and all of these solutions were washed out with DI water. Lastly, the substrates were placed under a compressed nitrogen (N<sub>2</sub>) flux for drying.

Finally, before spin casting of PEDOT:PSS and subsequent polymers, ITO/glass substrates were exposed to ultra violet (UV) radiation for approximately 10 minutes on a process call UV-ozone treatment in ambient atmosphere and room temperature. This procedure smoothes the ITO surface, which allows the formation of more uniform PEDOT:PSS films on it, enhancing its mobility. The UV-ozone treatment destroys organic residues on the surface as well.

### 3.3 DEVICE FABRICATION

#### 3.3.1 PREPARATION AND DEPOSITION OF THE POLYMER LAYERS

The PEDOT:PSS blend is the first polymer to be casted on the ITO/glass substrate. This was done through spin coating technique. Approximately, 900 µl of this solution was spin coated on the substrate at 3000 rpm for one minute. This gives a ~35 nm PEDOT:PSS film. The frequency and time was held constant for all devices. Right after deposition, the

samples were transfer to a nitrogen atmosphere inside an Inertec<sup>®</sup> glovebox to prevent oxygen and water vapor infiltration. The rest of the fabrication process was done in this atmosphere. The PEDOT:PSS film was then annealed at 120 °C for ten minutes, which further eliminated water traces, drying and fixing the polymer to the ITO layer. Additionally, annealing spreads the polymeric chain system, which favors the electrical conduction of the layer. For following steps, it was necessary to let the sample cool down back to ambient temperature.

Next, the active layer is deposited. As described above, commercial P<sub>3</sub>HT:PCBM blend was used for this layer. To ensure homogeneity, the blend was kept under magnetic agitation for at least 12 hours prior to deposition. The process was the same described for the first layer: polymer solution spin coating was made at 1000 rpm for three minutes, which gives a 170±10 nm width active layer. Once again, an annealing process was done, 140 °C for ten minutes, for the same reasons.

Finally, the rear contacts were fabricated through thermal evaporation under vacuum conditions in an evaporation chamber. For this, the sample was transferred to another glovebox (Braun<sup>®</sup>) with the aid of a transportation custom made load lock to prevent air exposition. This glovebox is integrated with equipment for thermal evaporation, which is inside a vacuum chamber. In selecting the deposition area, a protecting mask was placed over the active layer. Low evaporation rates ( $\sim 2\text{Å/s}$ ) of metals are used for smooth deposition of the metal contact. Pressure inside the deposition chamber during evaporation was about  $3 \times 10^{-6}$  mbar. The final thickness of these contacts was approximately 30 nm for calcium and 70 nm for the aluminum. The final structure of the layers on the substrate containing the solar cells is depicted in Figure 21(a). After fabrication, samples were kept under N<sub>2</sub> atmosphere until the characterization process was concluded.

Figure 21 (b) presents a top view of the substrate with the solar cells on it. In this figure, the intersection area of the photolithography on the ITO layer and the thermal evaporation masking of the metal contacts gives the precise effective area for the solar cells on the substrate, which is approximately 0.045 mm<sup>2</sup>.

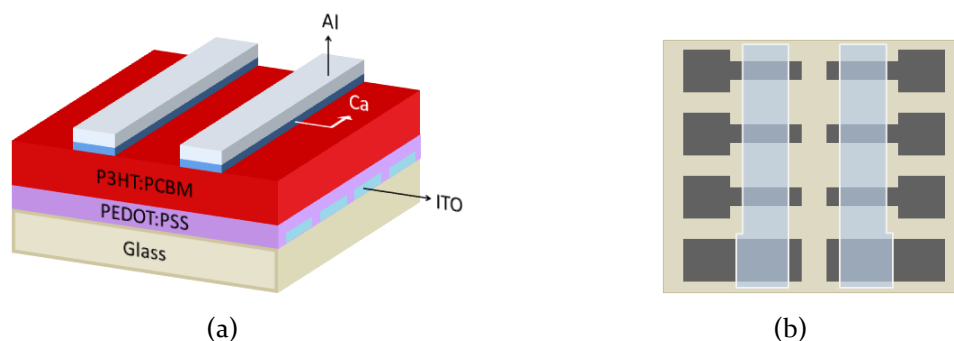


**Figure 21-** (a) Outline of the layer structure forming solar cells on substrates used in this work; (b) Diagram showing the intersection between the ITO and metal contacts on one substrate, which defines the effective area of each solar cell. There are six solar cells and two ground contacts on each substrate.

### 3.3.2 GOLD ION IMPLANTATION: MODIFIED SOLAR CELLS.

Bulk heterojunction solar cells with *modified* PEDOT:PSS layer were also fabricated. Actually, three of the six solar cells on the substrate shown on Figure 21 were made with a previously treated PEDOT:PSS layer, in a modification process described below.

Low energy metal ion implantation was performed on photolithographed ITO/glass substrates coated with PEDOT:PSS. The substrates were carefully masked to prevent implantation on the right half of the layer (Figure 22(a)). Gold ions were incorporated into the samples by means of the *Metal Plasma Immersion Ion Implantation & Deposition* (MEPIID) facility in our laboratory<sup>47</sup>. Cathodic arc gold plasma is formed in a vacuum plasma gun and it is directed toward substrate through the axial magnetic field of the bent-solenoid filter (Figure 22(b))<sup>48</sup>. Plasma gun consists of a cylindrical metal (in this case gold) cathode electrically isolated from the cylindrical anode around it. When a voltage difference is applied, electrical discharges are originated at non-stationary points on cathode's surface called cathodic spots. These discharges or *break downs* reach the anode surface, which acts as an electron collector. This way, plasma is produced. A solenoid around the plasma gun (not shown in Figure 22), connected in series with it, focus the plasma into penetrating the bent-solenoid filter. The filter removes non plasma components from the plasma stream, so that flux reaching the substrate is pure plasma. No acceleration voltage is applied on the substrate.

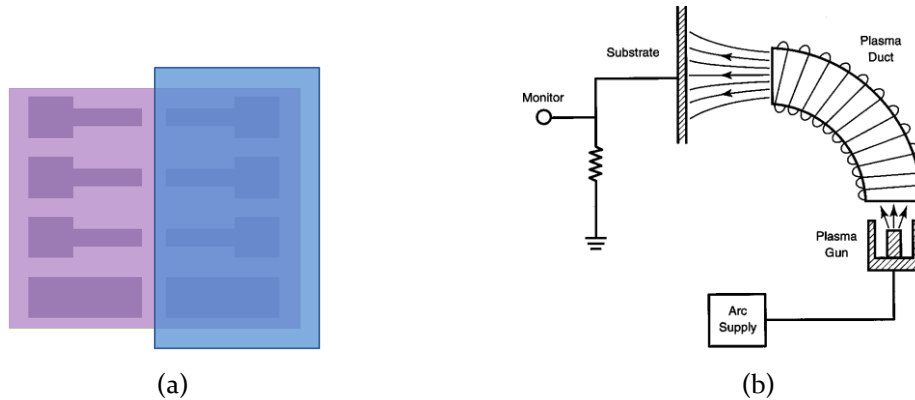


**Figure 22-** (a) top view of masking process of the PEDOT:PSS film on ITO/glass substrate for ion implantation. Only 3 of 6 solar cells are modified during this procedure; (b) Schematic diagram of the low vacuum arc plasma deposition system (Adopted from 47).

The plasma gun is operated in a pulsed mode, with 5 ms pulses generated at a frequency of 1 Hz. It is known from literature <sup>49</sup> that gold plasma leaves the plasma gun with 49 eV drift energy. Since no acceleration is performed on the substrate, the plasma arrives at the substrate surface with this energy. This is why the ion implantation, in this case, is a low energy process. Pressure inside chamber was held under  $3 \times 10^{-6}$  mbar for all the experiments performed.

By masking the target, only three of the six solar cells in the substrate are modified. As a result, reference and modified solar cells are fabricated in the same substrate, as can be seen in Figure 23. Except for the Au implantation, these cells were manufactured in the very same processes (spin substrate preparation, polymers spin coating, thermal evaporation of the metals, etc.) followed in non-modified solar cells. This feature eliminates discrepancies in the cells performances due to morphological differences from the fabrication process. In other words, any variation observed in the performances of reference and modified cells should be caused by the gold ion implantation. This is of great importance for characterization and analysis.

Along with PEDOT:PSS samples, crystal silicon substrates were incorporated inside the MEPIIID to be implanted during each implantation process. These samples were used to determine the actual implantation dose applied on each experiment through Rutherford backscattering spectrometry (RBS) (see section 3.4.2 and 4.1).

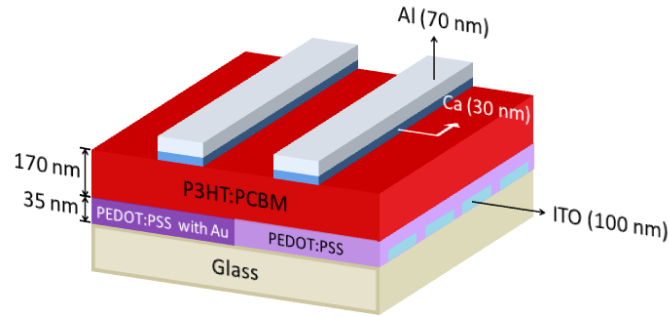


**Figure 23-** Final architecture of the layers forming the modified and non-modified solar cells investigated in this work.

### 3.3.3 DEVICES USED IN THIS WORK

The final array implemented for solar cells studied in this work is shown in Figure 23. Reference and modified solar cells are obtained in the same substrate as a result of the fabrication process followed. Shape and relative positioning of the ITO contacts and its intersection with metal contacts can be seen in Figure 20(f) and Figure 21(b).

Two separate experiments, with the features described in previous sections but carried out in different periods of time were performed. In each of these experiments, called A and B, two different doses were implanted on the PEDOT:PSS films, for a total of four implantation doses studied in this work. Controlled exposition times allowed varying the dose magnitude, which was kept around  $10^{15}$  atoms/cm<sup>2</sup>. Final doses values were obtained through RBS technique. The number of cells for each dose and the doses values themselves are shown in Table 2.

Experiment	Sample Designation	Number of solar cells		Au implantation dose (atoms/cm <sup>2</sup> )
		Reference	Modified with Au	
A	A1	9	7	$3.1 \times 10^{15}$
	A2		5	$6.4 \times 10^{15}$
B	B1	13	8	$2.1 \times 10^{15}$
	B2		6	$9.1 \times 10^{15}$

**Table 2-** Gold implantation doses implemented in this work. The number of references as well as modified cells for each implantation dose is showed.

### 3.4 SOLAR CELLS CHARACTERIZATION

#### 3.4.1 FILM ANALYSIS

##### (I) - ABSORPTION MEASUREMENTS

Absorption spectra of PEDOT:PSS films on ITO/glass substrates before and after gold implantation were made in a UV/Visible Hitachi® Spectrophotometer, model U-2900 at the *Grupo de Polímeros Prof. Bernhard Gross*, in the *Instituto de Física da USP- São Carlos*. It measures the absorbance of samples as a function of wavelength, using the visible, near ultraviolet and near infrared parts of the electromagnetic spectrum (190 nm to 1100 nm). Mathematically, absorption is defined by the Beer-Lambert law as:

$$A = -\log(Tr) = \log\left(\frac{I_0}{I}\right) \quad (3.1)$$

where  $A$  is the measured absorbance (in Absorbance Units - AU),  $Tr = I/I_0$  is the transmission,  $I_0$  and  $I$  are the intensity (power per unit area) of the incident and the transmitted light, respectively.

##### (II) - SCANNING ELECTRON MICROSCOPY IMAGES

Field Emission Scanning Electron Microscopy (FESEM) micrographs of the samples were done with a INSPECT F50 Field Emission Gun (FEG) – SEM microscope from FEI® at the *Instituto de Física de São Carlos*. Scanning electron microscopy (SEM) is a technique that scans a sample with an electron beam, and its interaction with the atoms on the surface generates various signals that can be detected and interpreted as surface topography or composition. In a typical SEM this electron beam is generated by thermionic emission at an electron gun cathode (for instance, a tungsten filament). In a FESEM, the electron beam is produced at a field-emission cathode, which uses an electrostatic field (rather than heat) to pull out the electrons. This provides narrower beams at low as well as high electron energies, resulting in improved spatial resolution and minimizing sample charging and damage.

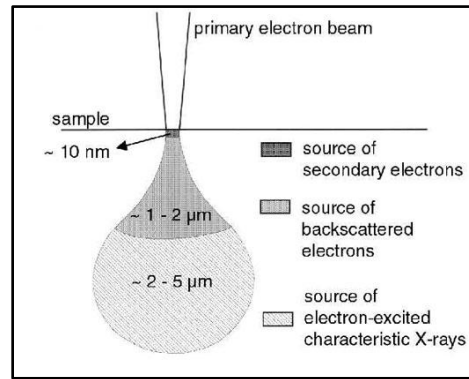


**Figure 24-** Electron beam interaction volume inside the material. Secondary and back-scattered electrons, as well as characteristic X rays are signals generated within different regions inside the sample.

The most common signals produced by a SEM include secondary electrons, back-scattered electrons and characteristic X-rays. Energy and interaction volume (Figure 24) inside the material are some of the characteristics that differentiate these electron signals. For the micrographs obtained in this work back-scattered electron signals were implemented. They consist of high energy electrons from the original beam that are back-scattered out of the specimen interaction volume (Figure 24) by elastic interactions with the sample atoms. Since high atomic number elements backscatter electrons more strongly than lighter elements, back-scattered electrons are used to make better contrast in regions with different chemical composition. Higher atomic number elements appear brighter in the back-scattered electrons images.

### (III) - FILM THICKNESS

Thickness of all polymer layers and metal contacts was measured by means of a Dektak II profilometer from VEECO® at the *Grupo de Polímeros Prof. Bernhard Gross*. This type of equipment possesses a diamond-tip stylus that is constantly touching the sample surface as it moves. The stylus is mounted on an arm coupled to a linear variable differential transformer (LVDT) that provides a DC signal proportional to the stylus displacement. A constant force on the stylus is maintained as the sample stage moves the sample under the stylus tip. Mechanical changes that occur whenever the stylus moves up or down are recorded as changes in the DC voltage signal. An altitude profile as the one shown in Figure 25 is traced and layer thickness is determined.

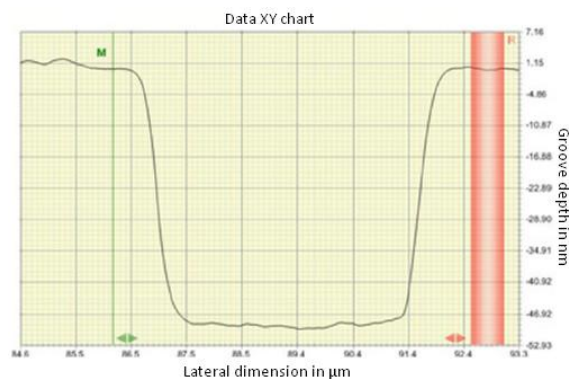


**Figure 25-** Typical altitude profile created by Dektak II profilometer from VEECO, used for measuring thickness of polymer and metal layers in this work.

### 3.4.2 RUTHERFORD BACKSCATTERING SPECTROMETRY (RBS)

RBS is a widely used technique in thin film analysis to determine elemental depth profiles and composition<sup>50</sup>. It uses high energy ion beams (usually  $\text{He}^+$  or  $\text{He}^{2+}$ ) to bombard the atoms in the target sample. The ion beam energies range from tenths of MeV to a few MeVs. On each collision, energy is transferred elastically from the incident ion to the stationary atom. The energy lost by the ion on this collision is proportional to the ratio of masses of the incident ion and the atom in the target. A detector records the energy for all backscattered ions and the identity of the species in the target is determined. Once identified, the density ( $\text{atoms}/\text{cm}^2$ ) of target atoms can be calculated from the probability of the collisions between them and incident ions occurs. This probability is estimated with the ratio of backscattered ions collected in the detector to the number of incident ions.

Silicon substrates were placed next to the PEDOT:PSS samples inside the MEPIIID during implantation procedure made on PEDOT:PSS films. RBS analysis were performed on these Si samples at *Laboratório de Análises de Materiais por Feixes Iônicos (LAMFI)* facilities in the *Instituto de Física da USP (IFUSP)* to determine the actual gold implantation doses implemented in this work.  $\text{He}^+$  ions with incident energy of 2.2 MeV were used. Simulation and analysis of RBS spectra obtained in this experiments as well as final calculation of the implanted dose in samples was done with the aid of the RBS analysis package RUMP-Rutherford Universal Manipulation Program. A typical RBS spectrum of Au implanted Si substrates as well as a simulation spectrum used for analysis is shown in Figure 26.

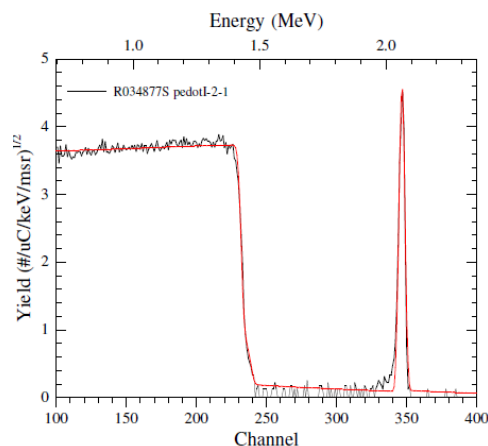


**Figure 26-** RBS spectrum of gold implanted Si substrates obtained during RBS analysis (black) and RUMP simulation used for analysis (red).

### 3.4.3 SRIM AND TRIDYN SIMULATIONS

Estimations of range profiles of implanted gold ions into PEDOT:PSS were performed with the use of TRIDYN and SRIM softwares. SRIM (*Stopping Range of Ions in Matter*) is an open source software package which estimates the projected range of ions inside matter using statistical algorithms and quantum mechanics<sup>51,52</sup>. TRIDYN (Transport and Range of Ions in Matter - TRIM including dynamic composition changes) is dynamic simulator based on the sputtering version of the TRIM program for multicomponent targets, which has become a widely used Monte Carlo simulation program to compute range profiles of implanted ions, composition profiles of the target and sputtering rates for a dynamically varying target composition. It takes into account compositional changes produced in the target after penetration of each implanted ion. A licensed version for our lab was provided in 2008 by Institute of Ion Beam Physics and Materials Research of Forschungszentrum Dresden-Rossendorf, Germany.

### 3.4.4 CURRENT -VOLTAGE CHARACTERISTICS

Terrestrial measurements of solar spectra vary depending on several aspects: latitude, weather conditions, time of day, etc. As it passes through the atmosphere, sunlight is attenuated by scattering and absorption of atoms in it. The more it travels, the more it interacts with the surrounding atoms. Finally, the sunlight intensity and

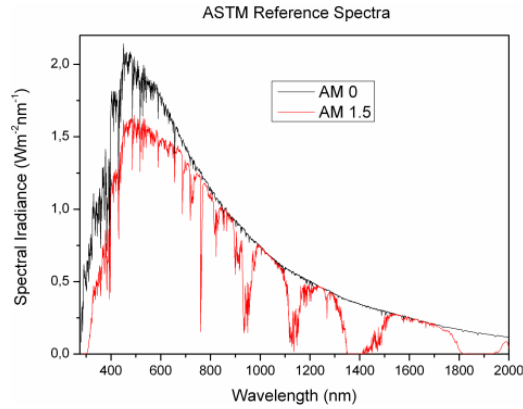


**Figure 27-** Solar radiation spectrum: right outside earth’s atmosphere (AM 0) and at a point on the earth’s surface where, having entered the atmosphere at an certain angle, the sunlight had crossed 1.5 atmospheres (AM 1.5). (Adopted from 53)

frequency arriving the earth’s surface depends very much on the path it followed (Figure 27). This is a hindrance for the photovoltaic research, since testing and comparison of solar cell performances depends entirely in its energy input: the sunlight. To solve this problem, the *American Society for Testing and Materials (ASTM)*, along with some of the most important photovoltaic research laboratories and the photovoltaic industry standardized the way the photovoltaic cells are tested and the results presented. They developed the “Terrestrial Reference Spectra for Photovoltaic Performance Evaluation”<sup>53</sup>, which indicates the intensity of the light and shape of the spectrum for solar cell characterizing. This reference spectrum is the AM 1.5 under a total irradiance of 100 mW/cm<sup>2</sup>. AM stands for “air mass” and refers to the *air mass coefficient*, a parameter that indicates the number of atmospheres the sunlight, having entered into the atmosphere at a certain angle, travels before hitting the earth’s surface (Figure 28). Thus, AM 0 means the sunlight has crossed zero atmospheres, i.e., hasn’t penetrated it yet. This is used as definition for the sunlight spectrum right outside the earth’s atmosphere. AM 1.5 means that sunlight has crossed one and a half atmospheres (see Figure 28). Mathematically:

$$AM = \frac{l}{l_0} \approx \sec \theta_z \quad (3.2)$$

where  $l$  is the path length through the atmosphere,  $l_0$  is the equivalent length of one atmosphere at sea level and  $\theta_z$  is the zenith angle (degrees). For AM 1.5 spectra  $\theta_z \approx 48.2^\circ$ , as shown in Figure 28.

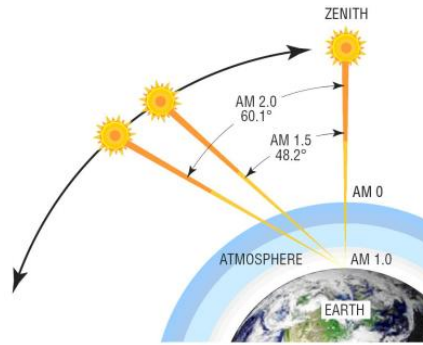


**Figure 28-** Definition of air mass coefficient AM. Sunlight entering the earth's atmosphere in angle can travel for a path length equivalent to more than 1 atmosphere (Adopted from the web).

Thus, solar spectrum simulation lamps nowadays must provide this type of spectrum. In characterizing the bulk heterojunction solar cells in this work, an Oriol<sup>®</sup> Xenon Arc Lamp Solar Simulator, which provides an AM 1.5 spectrum, was used. A calibrated silicon photodetector (Hamamatsu<sup>®</sup>) was employed to calibrate its spectral irradiance. Its power or total irradiance was calibrated at  $100\text{mW}/\text{cm}^2$  using an Ophir<sup>®</sup> power meter.

The current-voltage measurements were done by a 2400 Keithley<sup>®</sup> electrometer at the *Grupo de Polímeros Prof. Bernhard Gross*, in the *Instituto de Física da USP- São Carlos*. It was connected to a computer for data acquisition through a GPIB-USB-HS board from National Instruments<sup>®</sup>. All  $J_{xV}$  were taken for solar devices at room temperature and under a  $\text{N}_2$  atmosphere.

## CHAPTER 4

# RESULTS AND DISCUSSION

The effects of noble metal nanostructures, especially gold nanoparticles (AuNPs), in organic solar cells have been subject of great amount of research in the literature. Enhanced photon absorption by localized surface plasmons (LSPs)<sup>54-59</sup>, stable anode/active layer interfaces due to reduced chemical interactions<sup>60-62</sup>, reduced hole-transporting/active layer (HTL/AL) interfacial resistance provided by increased interfacial areas and/or effective energy level alignment and enhanced bulk conductivity of HTLs<sup>63,64</sup> are some of the mechanisms proposed to understand the effects of metal nanostructures in organic photovoltaic devices. This work is analyzed in the context of these and other effects.

As indicated in previous chapters, P3HT:PCBM BHJ solar cells modified through gold ion implantation in the HTL are analyzed in this work. The performance of reference and modified devices was followed in two separate experiments, each of them with two different implantation doses groups, for a total of four groups of cells with different implantation doses each. The number of devices implanted and implantation doses values, as well as the nomenclature used throughout this chapter was established in Table 2, section 3.3.3. Architecture and thickness of layers in reference and modified solar cells are shown in

Figure 21. Methods of characterization were described in the previous chapter. It was found that performance of solar cells was quite dependent not only on the amount of gold dose implanted, but also on the experiment process (A or B) each of them belong.

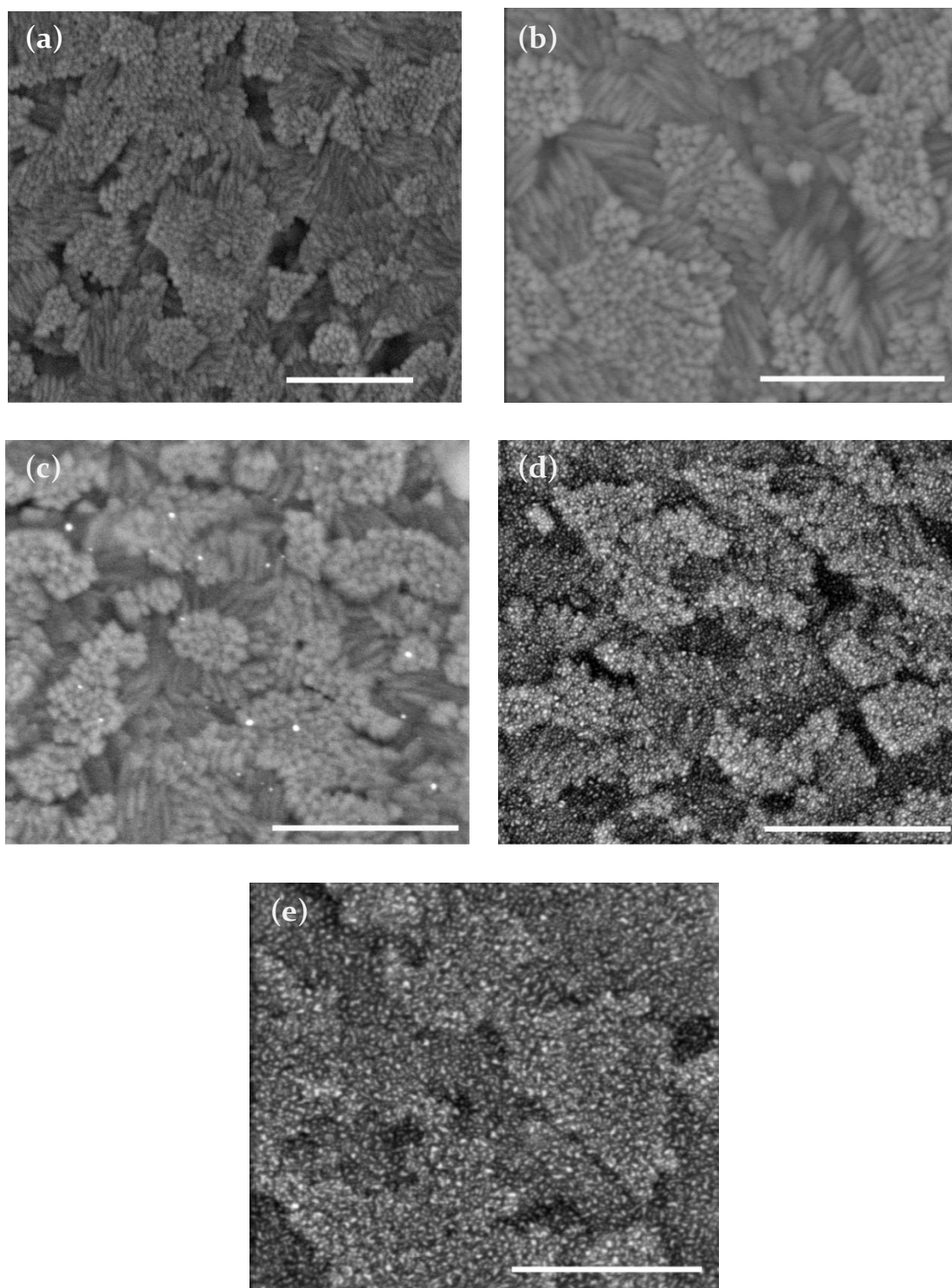
#### 4.1 RESULTS FROM RBS ANALYSIS

Table 2 in chapter 3 summarized the results from the RBS analysis on the implanted crystal silicon substrates putted inside the MEPIIID along with PEDOT:PSS samples, that determined the actual gold implantation dose (atoms/cm<sup>2</sup>) embedded in PEDOT:PSS of modified solar cells. With the aid of software package RUMP, doses values were calculated within an error of 6%. All of the doses were in the order of  $\sim 10^{15}$  atoms/cm<sup>2</sup>.

#### 4.2 FESEM IMAGES

The structures that gold ions implanted on PEDOT:PSS formed inside these films were investigated by means of a field emission scanning electron microscopy (FESEM). Results are shown on Figure 29. For the scanning, an electron beam of 15 keV was implemented and backscattered electron signal was recorded. As said before, elements with higher atomic number scatter electrons more effectively due to its higher atomic mass. Hence, more backscattered electrons come from heavier atoms increasing the signal recorded from them. This appears as brighter pixels in the FESEM micrographs.

Figure 29 shows the corresponding images of a PEDOT:PSS layer before and after implantation for the four different doses performed. As expected for the large electron beam energy used in this experiment, pristine PEDOT:PSS is transparent on this images and remains unseen (Figure 29(a)). Instead, the characteristic flakes of the underlying ITO are apparent (see appendix and reference 65). Furthermore, FESEM micrographs for B<sub>1</sub> samples (Figure 29 (b)) do not reveal an apparent difference from the previous one. It seems that either implantation dose is too low for gold atoms to precipitate, remaining isolated from each other in a gold-polymer solution in the PEDOT:PSS layer, or atoms do precipitated but the nanoparticles formed were below the FESEM resolution. In either case, no gold nanoparticles could be detected by FESEM.



**Figure 29-** FESEM micrographs of PEDOT:PSS coated ITO substrates: (a) before implantation; and after implantation of dose: (b) B1 ( $2.1 \times 10^{15}$  atoms/cm<sup>2</sup>), (c) A1 ( $3.1 \times 10^{15}$  atoms/cm<sup>2</sup>), (d) A2 ( $6.4 \times 10^{15}$  atoms/cm<sup>2</sup>) and (e) B2 ( $9.1 \times 10^{15}$  atoms/cm<sup>2</sup>). Formation of gold nanoparticles for implantation values  $\geq 3.1 \times 10^{15}$  atoms/cm<sup>2</sup> (c) is noticeable. Density of these AuNPs increases as implantation dose is enhanced, as seen in (d) and (e). The white bar represents 400 nm length.

A notable difference is shown on Figure 29(c) through (e). Figure 29(c) shows the FESEM micrograph of A1 samples, where low density gold nanoparticles (AuNPs) formed inside the PEDOT:PSS film are visible as bright white dots. From Table 2 is possible to know that the minimum implantation dose value required to observe AuNPs with the FESEM in this experiment was  $3.1 \times 10^{15}$  atoms/cm<sup>2</sup>. The total number of gold atoms exceeds the solubility limit of the PEDOT:PSS matrix and leads to nucleation and growth of AuNPs<sup>66</sup>. The AuNPs nucleate near the maximum of the implantation depth profile (next section). As expected, the density of AuNPs in the PEDOT:PSS layer increases for larger implantation doses, as it can be seen from Figure 29(d) and (e) for samples A2 and B2, respectively.

### 4.3 SRIM - TRIDYN SIMULATIONS

Range profiles of implanted ions were obtained through TRIDYN simulation program. For the extremely low ion energy used in this work (49 eV), shallow gold implantations in the PEDOT:PSS films were estimated. The simulations are shown on Figure 30. The maximum gold concentration in the PEDOT:PSS is found to be at a depth of ~3 nm underneath the surface. This is the *projected range* or maximum implantation depth profile. Au atomic fraction varies from ~0.2 for samples with lowest implantation (B1) to ~0.55 for highest implantation doses (B2). Similar projected ranges were obtained from the SRIM software. Thus, from Figure 29 and Figure 30 is possible to say that a thin layer of AuNPs right below PEDOT:PSS surface was obtained.

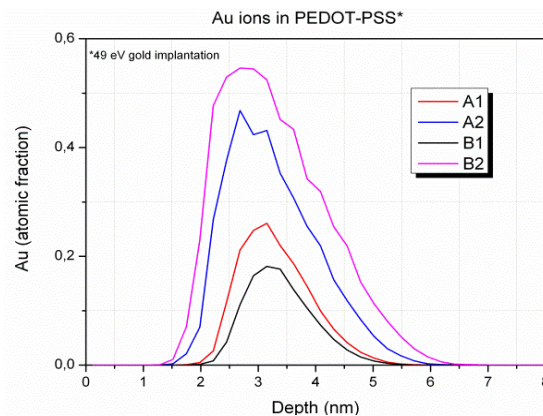


**Figure 30-** Simulation of the depth profile of Au implanted PEDOT:PSS for the ion energy of 49 eV and doses used in this experiment, as calculated by the TRIDYN simulation code.

#### 4.4 ABSORPTION MEASUREMENTS

Absorbance measurements of 35 nm thick PEDOT:PSS films over ITO coated glass (identical to those used for photovoltaic devices) before and after gold implantation further confirms the formation of AuNPs inside this layer. Results are presented on Figure 31. The pristine PEDOT:PSS over glass was used as the baseline. From Figure 31(a) it can be seen how the absorbance curves from samples B<sub>1</sub>, with lowest gold density, does not differ much from the baseline curve, basically showing the same absorption, which is in accordance with the FESEM results. As the gold implantation dose increases, the absorbance for all wavelengths increases, as expected too.

In order to obtain more information from the absorbance curves is necessary to determine the absorbance of the gold nanostructures alone, since curves in Figure 31(a) show the absorbance not only of implanted gold but of PEDOT:PSS layer and substrate as well. This is done by subtracting the baseline curve (pristine PEDOT:PSS) from all the absorbance curves from implanted samples. Then, the gold nanostructure “contribution” to the absorbance is obtained. The results are shown on Figure 31(b). These curves show a small wide peak centered approximately at: 470 nm for B<sub>1</sub>, 500 nm for A<sub>1</sub>; and just over 580 nm for A<sub>2</sub> and B<sub>2</sub>. This peak gets less pronounced for these latter samples as well.

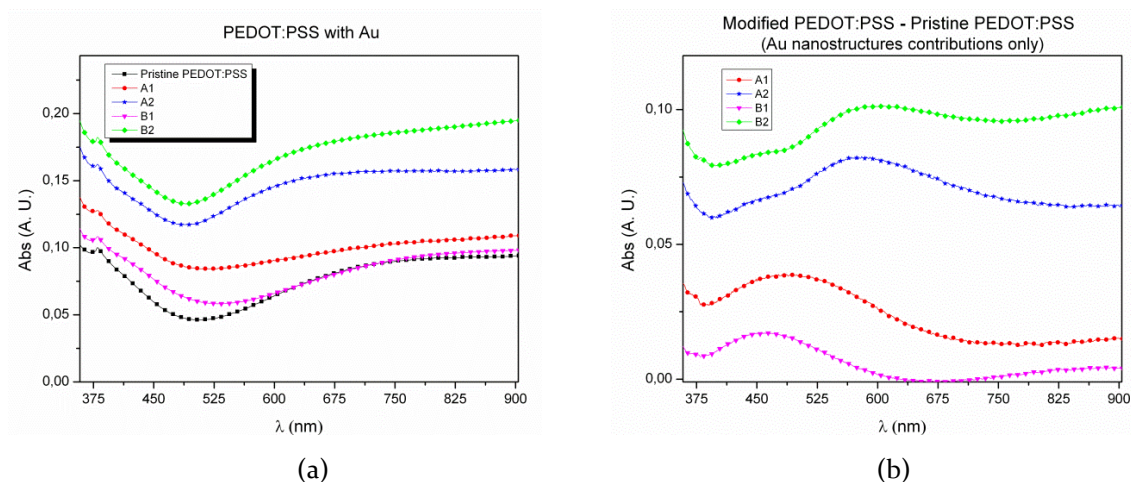


**Figure 31-** (a) Representative curves of the absorbance measurements of PEDOT:PSS films over ITO coated glass before (pristine PEDOT:PSS) and after gold implantation for several doses; (b) each of the curves presented in (a) minus the baseline curve (Pristine PEDOT:PSS line); which gives the absorbance of the implanted gold nanostructures alone.

Is known from literature<sup>54-57,59</sup> that peak formation around 500-600 nm in the absorption curves of gold nanostructures represents formation of nanoparticles. This has been widely investigated<sup>54-59</sup> as AuNPs can enhance photon absorption by localized surface plasmons, which in turn improves exciton creation and ultimately short circuit currents values.

## 4.5 CURRENT-VOLTAGE CHARACTERISTICS

Current-Voltage ( $JxV$ ) characteristics were obtained following the procedure described in chapter 3. In dealing with data from several devices (Table 2) a statistical approach was taken, meaning final results given for each parameter correspond to the average from results of individual solar cells on each experiment. The results are summarized in in Table 3 and Table 4 in the next sections.

### 4.5.1 REFERENCE SOLAR CELLS

$JxV$  curves for representative reference<sup>xiii</sup> cells from both experiment A and B are presented in Figure 32. These results exposed the great divergence that existed between the two experiments. Figure 32(a) shows the  $JxV$  measurements for the cells in the dark. Although dark  $JxV$  do not provide information regarding short circuit current, valuable data about the other parameters that dictate the electrical performance of solar cells can be obtained. As mentioned in section 2.6, an ideal solar cell in the dark should have a diode current-voltage behavior. Under forward bias, the current density in control A cells increases more rapidly than control B devices (Figure 32(a)). According to sections 2.4 and 2.5, once the bias exceeds the built-in electric field in the device at the *activation diode voltage* (proportional to the open circuit voltage  $V_{oc}$ ), injected current  $J_D$  grows exponentially in an ideal diode. Even when there could be a debate on whether or not control A cells are the only ones following a diode behavior in Figure 32(a), it is clear that the current density

---

<sup>xiii</sup> The terms *reference* and *control* solar cells are used indistinctively throughout this chapter when referring to solar cells without gold implantation.

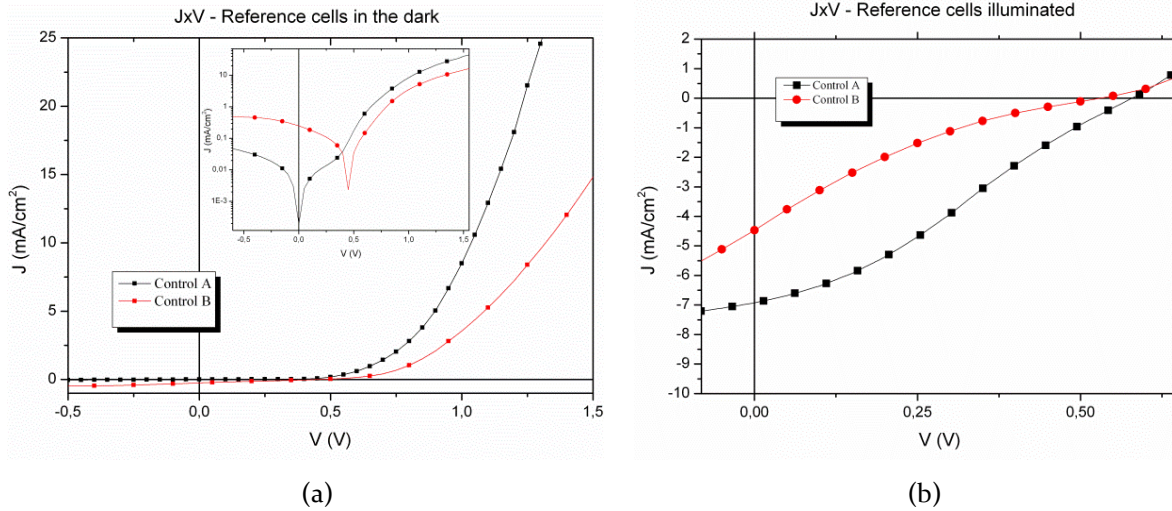


**Figure 32-**  $JxV$  characteristics for reference solar cells from experiments A and B: (a) in the dark (inset shows the semi-log scale); (b) under AM 1.5 illumination. Significant differences in photovoltaics parameters from experiments are evident.

in control B cells shows a much lower slope than control A devices. The reason for this may be larger series resistance  $R_s$  in control B cells. Large  $R_s$  diminishes charge injection and drifting in the device, which enhances charge recombination and ultimately holds back the exponential growth of  $J$ . Furthermore, as explained in section 2.6, high values of  $R_s$  reduce the short circuit current of the cell, which is in agreement with the  $J_{sc}$  values shown by  $JxV$  curves for the same devices under illumination (Figure 32(b)).

As was also mentioned, for zero voltage shouldn't be current flow in dark  $JxV$  characteristics; any current present is a leakage current, which are related to the  $R_p$ . In the semilog scale of dark  $JxV$  curves shown inset of Figure 32(a), it is clear that the current densities at  $V=0$  for control A cells,  $\sim 2 \times 10^{-4}$  mA/cm<sup>2</sup>, are about three orders of magnitude lower than control cells from B,  $\sim 2 \times 10^{-1}$  mA/cm<sup>2</sup> values. This indicates higher  $R_p$  values for control A cells. Additionally, reverse voltage should present saturation current  $J_o$  (see equations (2.9) and (2.10)) near zero and higher currents would also be a leakage currents, again related to the  $R_p$ . In the inset of Figure 32(a) a larger dark saturation current for control B cells is evident,  $J_o$  continues to grow as increasing reverse bias is applied, suggesting that control B cells have lower parallel resistances. This is confirmed, on Figure 32(b), by the higher slope near  $J_{sc}$  of illuminated  $JxV$  curves from control B cells. Finally, the  $V_{oc}$  can also be affected by lower  $R_p$ , although slightly.

In summary, reference cells from experiment A showed better overall performances compared to those in experiment B. Lower series resistances  $R_s$ , higher open circuit voltage, higher short circuit current and higher parallel resistance lead to  $JxV$  curves with better field factor (as expected from the shape of  $JxV$  in Figure 32(b)) and ultimately to better efficiency, as shown in Table 3 and Table 4.

Since both modified-though-gold-implantation and reference solar cells were manufactured on the same substrates, at the same time and through the exact same process for both experiments (chapter 3), is reasonable to expect the same discrepancies shown by the  $JxV$  characteristic of control devices to arise in the modified devices as well. Thus, comparisons between modified cells from different experiments are not meaningful; instead, performances of modified solar cells must be weighed solely against those of reference cells from the same experiment. Only the relative variations can be compared between experiments. This approach will be followed hereafter.

#### 4.5.2 EXPERIMENT A

Figure 33 shows the  $JxV$  curves in the dark and under AM 1.5 illumination for typical modified (A1 and A2) and control solar cells from experiment A. As described in the previous section and as can be seen in Figure 33(a), the higher slope in dark  $JxV$  characteristics of modified cells under forward bias indicates lower series resistance. This was confirmed in the illuminated curves (Figure 33(b)), clearly showing a steeper slope around open circuit voltage, which indicates low  $R_s$  according to section 2.6. Calculations made from Figure 33(b) showed an outstanding decrease of  $\sim 1$  of magnitude in the  $R_s$  of modified solar cells, dropping from  $\sim 152 \Omega\text{cm}^2$  for control cells down to  $\sim 15 \Omega\text{cm}^2$  and  $\sim 12 \Omega\text{cm}^2$  for samples A1 and A2, respectively. The reasons for such a reduction will be discussed in section 4.6. As said in the previous section, lower  $R_s$  can increase short circuit current  $J_{sc}$  values, as carrier recombination is reduced. A closer inspection of Figure 33(b) shows a small improvement in  $J_{sc}$ , specially for samples A1, which also will be discussed later on this chapter. Results for  $R_s$ ,  $J_{sc}$ , as well as  $V_{oc}$ ,  $R_p$ ,  $FF$  and efficiency from experiment A are summarized in Table 3.

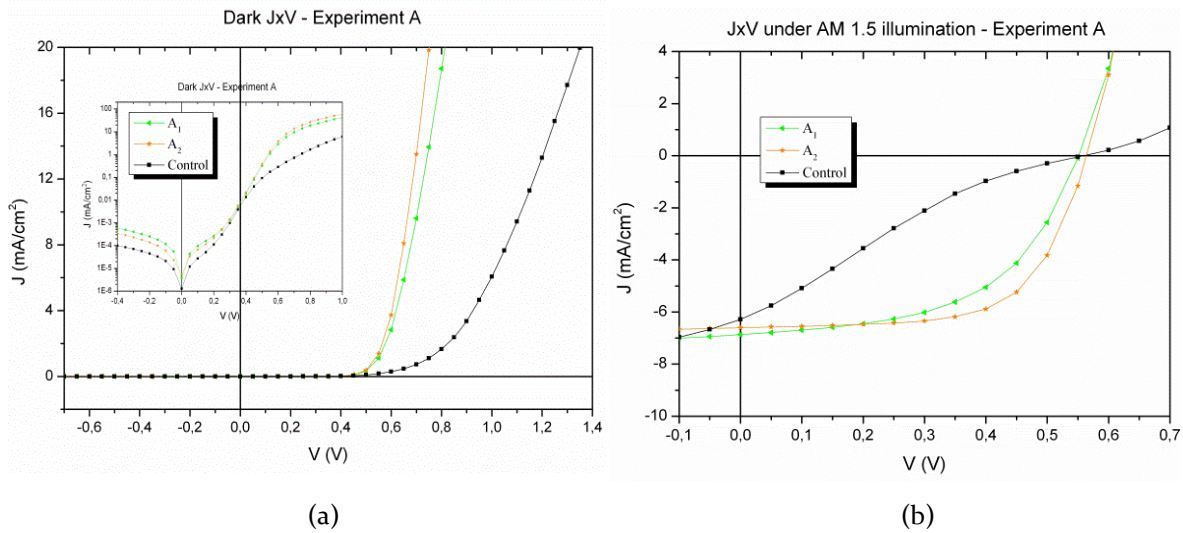


**Figure 33-** Typical  $JxV$  characteristics for modified and reference devices from experiment A: (a) in the dark; (b) under AM 1.5 illumination. Gold-implanted solar cells show better overall performance in comparison with control cells.

Analyzing the inset in Figure 33(a) higher dark saturation currents of modified A<sub>1</sub> and A<sub>2</sub> solar cells, compared to control cells, are apparent. Although  $J_0$  values from modified solar cells were slightly higher than control devices, the influence they exert on parameters  $R_p$  and  $V_{oc}$  is basically negligible as these parameters remained unaffected. On the contrary, they proved to be much larger in modified devices than in control cells, as can be deduced from the illuminated curves in Figure 33(b). Calculations showed that parallel resistance increases dramatically from approximately 200  $\Omega\text{cm}^2$  for reference devices up to  $\sim 900 \Omega\text{cm}^2$  and  $\sim 1520 \Omega\text{cm}^2$  for modified samples A<sub>1</sub> and A<sub>2</sub>, respectively. Also, the open circuit voltage showed no variation in comparison with control cells, within the margin of error, for A<sub>1</sub> or A<sub>2</sub>, remaining constant at approximately 0.55 V.

The final result of such improvements in the modified solar cells parameters is an impressive enhancement of the field factor  $FF$  and consequently of the power conversion efficiency  $\eta$  of the devices. Both were increased by a factor of more than 2, being 2.5 times better in the case of A<sub>2</sub> cells (with the highest implantation dose), the top performance devices in the experiment. Results for experiment A are summarized in Table 3.

Experiment A						
Sample	$J_{sc}$ (mA/cm <sup>2</sup> )	$V_{oc}$ (V)	$R_p$ ( $\Omega$ cm <sup>2</sup> )	$R_s$ ( $\Omega$ cm <sup>2</sup> )	FF	$\eta$ (%)
Control A	6.28 ( $\pm$ 0.35)	0.553 ( $\pm$ 0.019)	201 ( $\pm$ 41)	153 ( $\pm$ 23)	0.25 ( $\pm$ 0.02)	0.89 ( $\pm$ 0.12)
A1	7.00 ( $\pm$ 0.11)	0.558 ( $\pm$ 0.004)	927 ( $\pm$ 84)	15.3 ( $\pm$ 0.9)	0.56 ( $\pm$ 0.01)	2.17 ( $\pm$ 0.07)
A2	6.55 ( $\pm$ 0.05)	0.565 ( $\pm$ 0.004)	1518 ( $\pm$ 170)	12.6 ( $\pm$ 0.7)	0.61 ( $\pm$ 0.01)	2.26 ( $\pm$ 0.06)

**Table 3-** Average results obtained for modified and references solar cells parameters for experiment A. Outstanding improvements for devices with AuNPs are manifest.

#### 4.5.3 EXPERIMENT B

Figure 34 shows typical  $JxV$  characteristics of modified (B1 and B2) and control solar cells both in the dark and under AM 1.5 illumination found in this experiment. Again, lower series resistances for modified solar cells are expected due to the higher slope of  $J$  under forward bias in dark  $JxV$  characteristics (Figure 34(a)). Illuminated curves (Figure 34(b)) support this, as the steeper enhancement of  $J$  around open circuit voltage indicates low  $R_s$ , accordingly. Calculations made from Figure 34(b) showed a decrease in the  $R_s$  of modified solar cells in comparison with control cells, analogous with experiment A, of one order of magnitude.  $R_s$  dropped from  $\sim 300 \Omega\text{cm}^2$  for control cells down to  $\sim 40 \Omega\text{cm}^2$  and  $\sim 30 \Omega\text{cm}^2$  for B1 and B2 devices, respectively. This, once again, results in increased short circuit current  $J_{sc}$  values, with the difference this time the increment is very large, especially for samples B1, which were increased by a factor of 1.27. Solar cells parameters of devices in experiment B are summarized in Table 4.

The main difference between experiments A and B is the behavior of the saturation currents. Although  $J_o$  values for solar cells with AuNPs are surprisingly similar to those in experiment A ( $\sim 10^{-4}$  mA/cm<sup>2</sup>), the control devices are in this case the ones with higher  $J_o$ . According to section 4.5.1, this predicts higher  $R_p$  values for devices B1 and B2, which collaborates with the (already present) mechanisms from AuNPs in enhancing  $R_p$ . This prediction is confirmed in the illuminated  $JxV$  characteristics of Figure 34(b). As can be seen,  $R_p$  and  $V_{oc}$  are significantly incremented for B1 and B2 cells when compared to control devices.

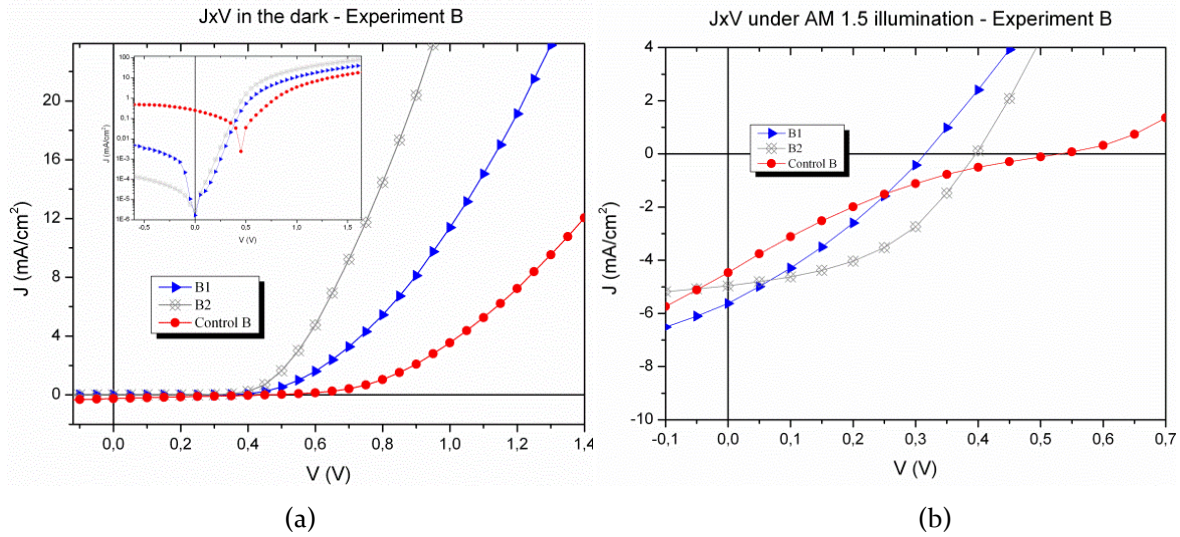


**Figure 34-** Typical  $JxV$  characteristics of control and modified solar cells from experiment B: (a) in the dark; (b) under AM 1.5 light. As in experiment A, AuNPs rectify the poor shape presented in illuminated  $JxV$  curves in control cells. As will be discussed in section 4.6, this poor shaped  $JxV$  are called S-shaped curves; which origins are analyzed.

Calculations based on curves from Figure 34(b) yielded  $R_p$  values from  $\sim 80 \Omega\text{cm}^2$  for reference devices,  $\sim 100 \Omega\text{cm}^2$  and  $\sim 400 \Omega\text{cm}^2$  for B1 and B2 cells, respectively. Nevertheless, the open circuit voltage was deteriorated for B1 and B2 cells, in comparison with control cells, as can be seen in Figure 34(b) and Table 2. The reason behind this is discussed in the next section.

The overall performance of cells modified with AuNPs was improved; as devices with improved field factors and, consequently, power conversion efficiencies were obtained. These results are summarized in Table 4. Top performance was shown by B2 modified cells.

Experiment B						
Sample	$J_{sc}$ (mA/cm <sup>2</sup> )	$V_{oc}$ (V)	$R_p$ ( $\Omega\text{cm}^2$ )	$R_s$ ( $\Omega\text{cm}^2$ )	FF	$\eta$ (%)
Control B	4.4 ( $\pm 0.3$ )	0.53 ( $\pm 0.01$ )	79 ( $\pm 5$ )	304 ( $\pm 31$ )	0.17 ( $\pm 0.01$ )	0.41 ( $\pm 0.03$ )
B1	5.6 ( $\pm 0.3$ )	0.31 ( $\pm 0.01$ )	95 ( $\pm 9$ )	39 ( $\pm 3$ )	0.30 ( $\pm 0.01$ )	0.53 ( $\pm 0.05$ )
B2	5.0 ( $\pm 0.4$ )	0.39 ( $\pm 0.02$ )	431 ( $\pm 57$ )	31 ( $\pm 4$ )	0.45 ( $\pm 0.02$ )	0.91 ( $\pm 0.14$ )

**Table 4-** Average results obtained for modified and references solar cells parameters for experiment B. Although the values are quite different, relative performance between experiment A and B is pretty similar.

#### 4.6 COMPARATIVE ANALYSIS OF EXPERIMENTS A AND B

Figure 33(b) and Figure 34(b) with the  $JxV$  characteristics of solar cells under AM 1.5 illumination revealed an important difference between performances of reference and modified devices that was consistent in experiments A and B. Control cells exhibited an abnormal S-shaped or *kink* current-voltage characteristics under illumination, which refers to the uncommon shape of  $JxV$  curve, deviating from the somewhat squared  $JxV$  curve typical cells make (see Figure 12, chapter 2). As a result, deteriorated parallel and series resistances were obtained for reference devices, along with significantly reduced field factors and power conversion efficiencies. Interestingly, this kink behavior was rectified in the gold-modified solar cells for both experiments (compare  $JxV$  curves of modified and control cells in Figure 33(b) and Figure 34(b)). Since control cells were prepared with pristine PEDOT:PSS on the same substrate and under the exact same conditions as gold implanted cells during fabrication and characterization (Chapter 3), the rectification of  $JxV$  characteristics is in all probability due to the presence of the AuNPs under the PEDOT:PSS surface. The overall result is a significant improvement of the efficiency for cells modified with gold (by a factor higher than 2 in most cases; see Table 3 and 4). It is worth to mention that  $JxV$  characteristics of control devices in the dark, in both experiments, do not show the S-shaped curve. This implies that the kink behavior is related to the photogenerated carriers.

S-shaped  $JxV$  curve has been subject of intense experimental and theoretical research and several explanations have been proposed for it. Among the most common are: interfacial dipoles<sup>67</sup>, charge accumulation<sup>68,69</sup>, contact degradation effects<sup>68,70-72</sup>, imbalanced mobilities between holes and electrons<sup>68,73</sup>, diminished charge extraction<sup>68,74</sup>, phase separation of the two organic components<sup>75</sup>, etc. Nonetheless, further experimental investigations are still necessary to confirm the origin of the kink  $JxV$  curve and to provide methods to consistently eliminate it.

To understand the reasons behind this behaviors in experiments A and B, the performances from control cells are analyzed first. For this, is necessary to review some of the steps taken during fabrication and characterization of the solar cells.

After deposition and annealing of PEDOT:PSS layer on ITO/glass substrates, samples were taken to the MEPIIID facilities for gold implantation. Although substrates were transferred inside a vacuum desiccator, a substantial period of time passed from PEDOT:PSS deposition until implantation process. This, along with the need to transfer the sample between different equipments and labs (see chapter 3) led to an exposition of the PEDOT:PSS samples to air, allowing water and oxygen molecules to penetrate it. The ability of PEDOT:PSS to absorb water and oxygen from the atmosphere are well known<sup>76-78</sup>. Koch and colleagues investigated the effects of oxygen and water on PEDOT:PSS, showing that water diffuses into PEDOT:PSS bulk increasing its electrical resistance<sup>76</sup>. This can provoke the appearance of insulating regions at the interface of PEDOT:PSS/Active-layer in solar cells, which decreases the charge collection efficiency<sup>60,76</sup>. Such insulating domains could result from the reaction of acidic species in PSS with water<sup>60,61</sup>. Furthermore, water absorption can reduce the work function of the PEDOT:PSS significantly<sup>76</sup>, increasing the energy barrier at its interface with the P<sub>3</sub>HT. In addition, water absorption also decreases the PSS concentration at the PEDOT:PSS layer surface leading to worst electrical contact at the interface with the P<sub>3</sub>HT<sup>76</sup>. Thus, hole collection at the anode is reduced, leading to (photogenerated) charge accumulation in the PEDOT:PSS/P<sub>3</sub>HT interface. Theoretical studies also suggest that charge accumulation in the PEDOT:PSS/P<sub>3</sub>HT:PCBM interface can increase the exciton recombination rate in the active layer<sup>69,70</sup>. These are all well known causes of S-shaped curves in BHJ solar cells. So, the blame for the kink performances of  $J \times V$  curves in control solar cells in both experiments is put in the water absorption and diffusion in the PEDOT:PSS layer.

As detailed previously, the performance of devices with AuNPs near the PEDOT:PSS surface were remarkably improved in experiments A and B, rectifying the abnormal behavior observed in the control cells (see Table 3 and Table 4).

Similar results were found in literature for CuPc:Fullerene based bilayer solar cells<sup>60</sup> and are shown in Figure 35 for comparison. Modification of the PEDOT:PSS/Active-layer interface with an ultra thin layer (~2 nm) of gold was also attributed for the rectification of S-shaped  $J \times V$  curves originated from exposure to air of the PEDOT:PSS. The behavior of

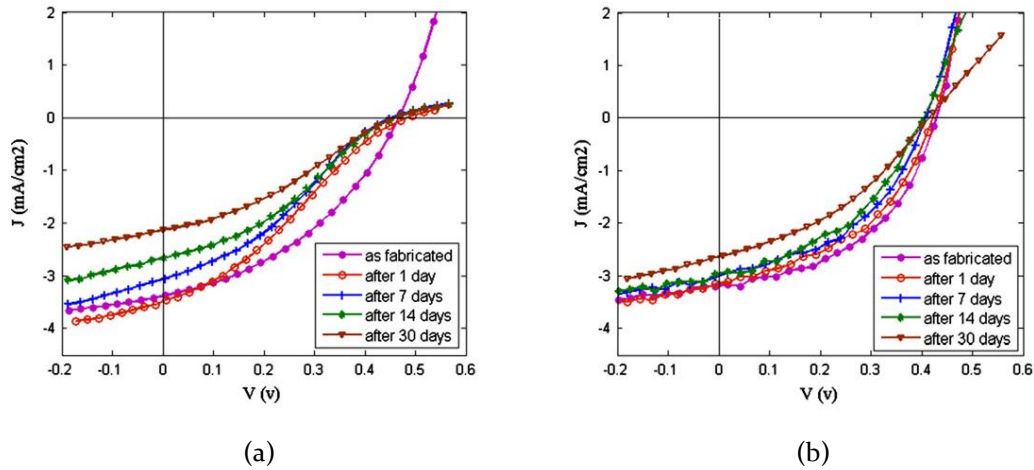


**Figure 35-** Literature results involving gold on PEDOT:PSS showing similar behavior for CuPc:Fullerene based bilayer solar cells <sup>60</sup>. Degrading effects of oxygen and moisture on the  $JxV$  characteristics of: (a) bilayer control solar cells; (b) Solar cell modified with an Au thin film in the PEDOT:PSS/Active-layer interface. S-shaped  $JxV$  in (a) are attributed to degradation of the PEDOT:PSS/Active-layer interface due to water diffusion into PEDOT:PSS. The gold thin film at the interface rectified the S-shape of the  $JxV$  and dramatically decelerated the degradation process.

devices modified with gold is compared to control cells when both are exposed to oxygen and humidity for different periods of time. The stability improvement provide by the gold thin layer in the cells was ascribed, to the “prevention from the reduction in anode work function with the lapse of time” and the “possible protective ability of Au layer against permeation of water into the PEDOT:PSS” <sup>60</sup>, among others. Similar effects are believed to occur in this work.

The most important mechanism that AuNPs can be exerting on the devices is related to the work function of the PEDOT:PSS layer, which may have improved due to the presence of AuNPs. As seen in the Metal-Semiconductor junction model (section 2.7), the relationship between work functions of interfacing materials is crucial for the charge transport properties in this region. In first approximation, the PEDOT:PSS may be picture as a metal interfacing the organic semiconductor junction P<sub>3</sub>HT:PCBM. In the absence of AuNPs, the original work function of PEDOT:PSS (5.1 eV), could reduced significantly during oxygen and water exposure, as mentioned, enhancing the hole extraction energy barrier  $\Phi_{BS}$  between the  $n$ -type P<sub>3</sub>HT and the PEDOT:PSS (see equation 2.14) in control solar cells.

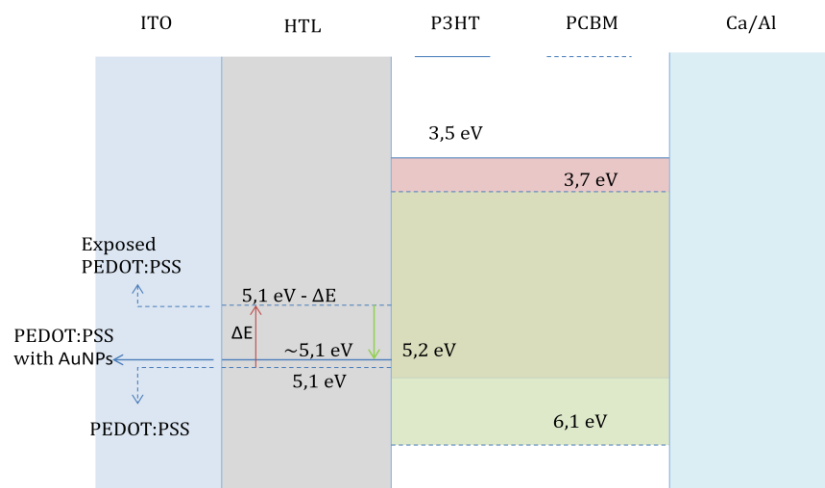


**Figure 36-** Energy band diagram of the process BHJ solar cells went through during these experiments, for the case of : control cells (with pristine PEDOT:PSS), which work function degrades upon air exposition (red arrow); and with modified PEDOT:PSS (with embedded AuNPs), which work function is rectified (green arrow).

This barrier hinders the hole transport within the device, diminishing collection at the anode. Holes would accumulate at the PEDOT:PSS/active-layer interface, creating regions with enhanced charge recombination rates in the P<sub>3</sub>HT:PCBM. Also, the electron blocking energy barrier between the *n*-type PCBM and the PEDOT:PSS is reduced (see equation 2.12), also incrementing charge recombination and undermining electron collection at the cathode. Both situations ultimately diminish the overall performance of the control solar cells through S-shape  $J \times V$  characteristics.

Modified PEDOT:PSS/P<sub>3</sub>HT interfaces with AuNPs can improve potential the potential barrier conditions due to the high work function of Au. Some reports state that the work function of clean Au is about 5.1 eV<sup>79</sup>, which is similar to that of the unexposed PEDOT:PSS. Placing the AuNPs near the surface of the PEDOT:PSS can increase or maintain its original work function. This rearranges the energy levels at this interface to a more favorable state: higher electron blocking and lower hole extraction barriers. The latter could even reestablished to an ohmic contact in the interface as a result<sup>63,64</sup>. Figure 36 outlines this energy levels alignment process.

As mentioned in previous sections, the series resistance  $R_s$  of samples with AuNPs reduced by a factor of 10, which can be attributed both to a reduced interfaced energy

barrier and better contact of the polymeric layers. Increased parallel resistance reveals a lower leakage of charge transporters, which can be attributed to a more uniform electric field in PEDOT:PSS layer due to the presence of AuNPs<sup>64</sup>. This effect makes a more favorable conduction pathway for the holes across the PEDOT:PSS. Although experimental measurements are necessary for confirmation, absorption measurements in Figure 31 suggest that the increasing in the short circuit current can be also attributed to enhanced photon absorption by localized surface plasmons in the PEDOT:PSS/P<sub>3</sub>HT:PCBM interface. As can be seen in Figure 31(b), the presence of AuNPs increases the absorption rate of the PEDOT:PSS layer. Since the AuNPs are placed right underneath the surface of the PEDOT:PSS, is believed this enhanced absorption field can reach the active layer and improve photon absorption and consequently exciton generation<sup>54</sup>.

# CONCLUSIONS

Fabrication, characterization and analysis of organic photovoltaic devices based on conjugated polymers were carried out in this work. The performance of P<sub>3</sub>HT:PCBM based bulk heterojunction solar cells modified through low energy gold ion implantation in the hole transporting layer (PEDOT:PSS) was analyzed in two separated experiments A and B. Reference cells without gold were also fabricated and characterized for comparison.

Through RBS analysis, the two different implantation doses performed on each experiment were calculated. Values were:  $3.1 \times 10^{15}$  atoms/cm<sup>2</sup> and  $6.4 \times 10^{15}$  atoms/cm<sup>2</sup> for experiment A;  $2.1 \times 10^{15}$  atoms/cm<sup>2</sup> and  $9.1 \times 10^{15}$  atoms/cm<sup>2</sup> for experiment B. Range profiles of implanted ions obtained with TRIDYN and SRIM simulation programs estimated shallow gold implantations of ~3 nm underneath the PEDOT:PSS films surface. Au atomic fractions calculated with TRIDYN varied from ~0.2 for samples with lowest implantation to ~0.55 for highest implantation doses. Field emission scanning electron microscopy (FESEM) micrographs showed the formation of gold nanoparticles in the PEDOT:PSS layer for the three highest doses used. Absorbance spectrum of PEDOT:PSS films before and after gold implantation further confirmed this.

$JxV$  characteristics of reference solar cells under AM 1.5 illumination presented the uncommon S-shaped curves, which refers to the abnormal deviation from the somewhat squared  $JxV$  curve typical functioning cells present. This kink behavior was attributed to PEDOT:PSS degradation due to oxygen and water exposure, provoking the appearance of insulating regions at the interface of PEDOT:PSS/Active-layer and reducing the work function of the PEDOT:PSS significantly, which increased the energy barrier for hole extraction efficiency at the interface and enhanced charge accumulation and exciton recombination in the PEDOT:PSS/P<sub>3</sub>HT. As a result, deteriorated parallel and series resistances were obtained in reference devices, along with significantly reduced field factors and power conversion efficiencies.

This kink behavior was consistently eliminated in both experiments with the introduction of AuNPs near the PEDOT:PSS/Active-layer interface. The illuminated  $JxV$  curves of modified solar cells were rectified and cell parameters reestablished. As a result, impressive upgrades of the field factors for modified solar cells in both experiments, which ultimately enhanced the efficiencies by a factor higher than 2 were obtained. This was attributed to improvement (and prevention from the reduction) of the PEDOT:PSS work function layer due to the presence of AuNPs, which rearranged the energy levels at the interface to a more favorable state: higher electron blocking and lower hole extraction barriers.

Although further experimental measurements are necessary for confirmation, absorption measurements suggest that the increasing in the short circuit current can be also attributed to enhanced photon absorption by localized surface plasmons in the PEDOT:PSS/P<sub>3</sub>HT:PCBM interface. Since the AuNPs are placed right underneath the surface of the PEDOT:PSS, is believed this enhanced absorption field can reach the active layer and improve photon absorption and consequently exciton generation.

## APPENDIX

# AFM IMAGES OF ITO/GLASS SUBSTRATES

The homogeneity of the indium-tin oxide (ITO) substrate surface was analyzed through *atomic force microscopy* (AFM) tapping technique in a Nanoscope IIIA Multimode microscopy from Digital <sup>®</sup>. Surface roughness was investigated. This was made as part of a broader interface analysis for charge carrier transport characterization between component layers of the BHJ solar cells studied in these experiments.

AFM is part of a larger family of microscopic techniques called *scanning probe microscopes* (SPM) <sup>80</sup>. The common characteristic these techniques possess is their capacity to study surface topography and properties of materials from the micron all the way down to the atomic level. This power of resolution is the most attractive feature SPM provides, which is possible due to two fundamental components present in SPM: the probe and the scanner. The probe scans the sample surface and records an interaction between them. This interaction could be an electrical or magnetic force, a tunneling current, a surface potential, etc. The resulting image can be understood as a surface map reflecting this interaction. The scanner is composed by a piezoelectric material that controls the precise position of the probe in relation to the surface. Together, the probe and the scanner are able to provide a

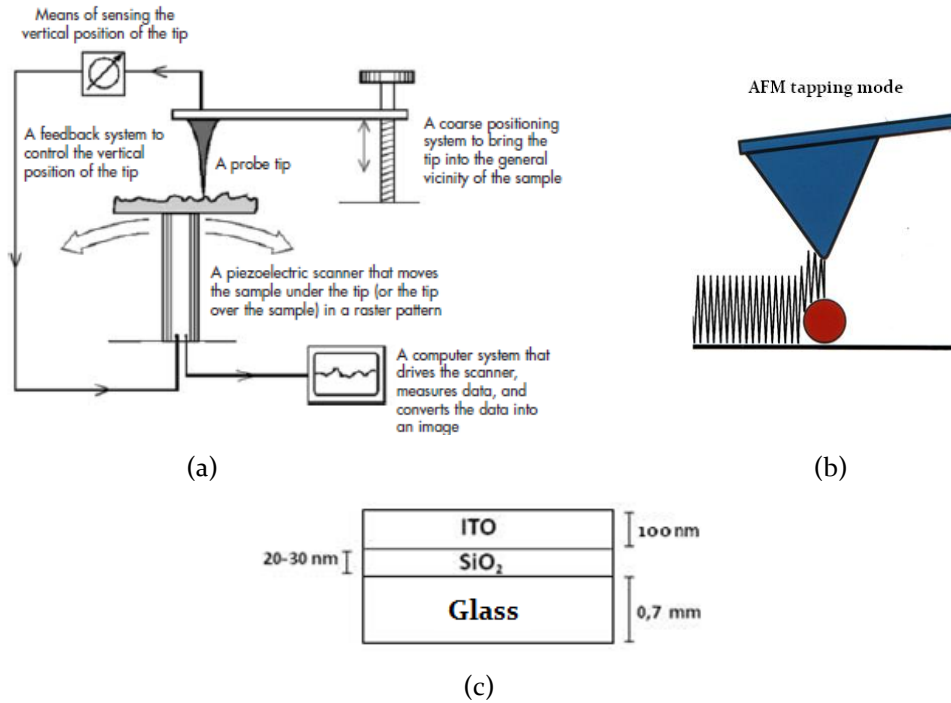


**Figure 37-** (a) Outline of the SPM working loop (Adopted from 80); (b) AFM tapping mode operation principle; (c) diagram of the ITO/glass samples analyzed in this experiment.

high resolution register of physical or chemical properties of the material. A basic design of SPM without reference to any specific technique is shown in Figure 37(a). The techniques implemented in SPM are named according the interaction each of them are capable of registering. Among the most common techniques there are the *Scanning Tunneling Microscopy* (STM) and the already mention AFM. Other modes of operation are: *Electric Force Microscopy* (EFM), *Magnetic Force Microscopy* (MFM), *Scanning Near-field Optical Microscopy* (SNOM), *Scanning Capacitance Microscopy* (SCM), *Scanning Ion Conductance Microscopy* (SICM).

The AFM technique, implemented in this experiment, maps the sample's topography by lightly tapping the surface with an oscillating probe tip (Figure 37(b)). The cantilever's oscillation amplitude changes with sample surface topography. The amplitude change is registered at each point of the surface and the image is produced. An outline of the ITO samples analyzed through this technique is shown in Figure 37(c). The commercially obtained ITO coated glass consists of a ~100 nm ITO layer over the SiO<sub>2</sub> passivated glass surface.

The resulting images from  $2\ \mu\text{m} \times 2\ \mu\text{m}$  AFM scans on one ITO sample are shown in Figure 38. A roughness analysis was performed for three different regions of each sample. The mean roughness  $R_{rms}$  of the ITO, which proved to be pretty homogeneous, was 4.06 nm.

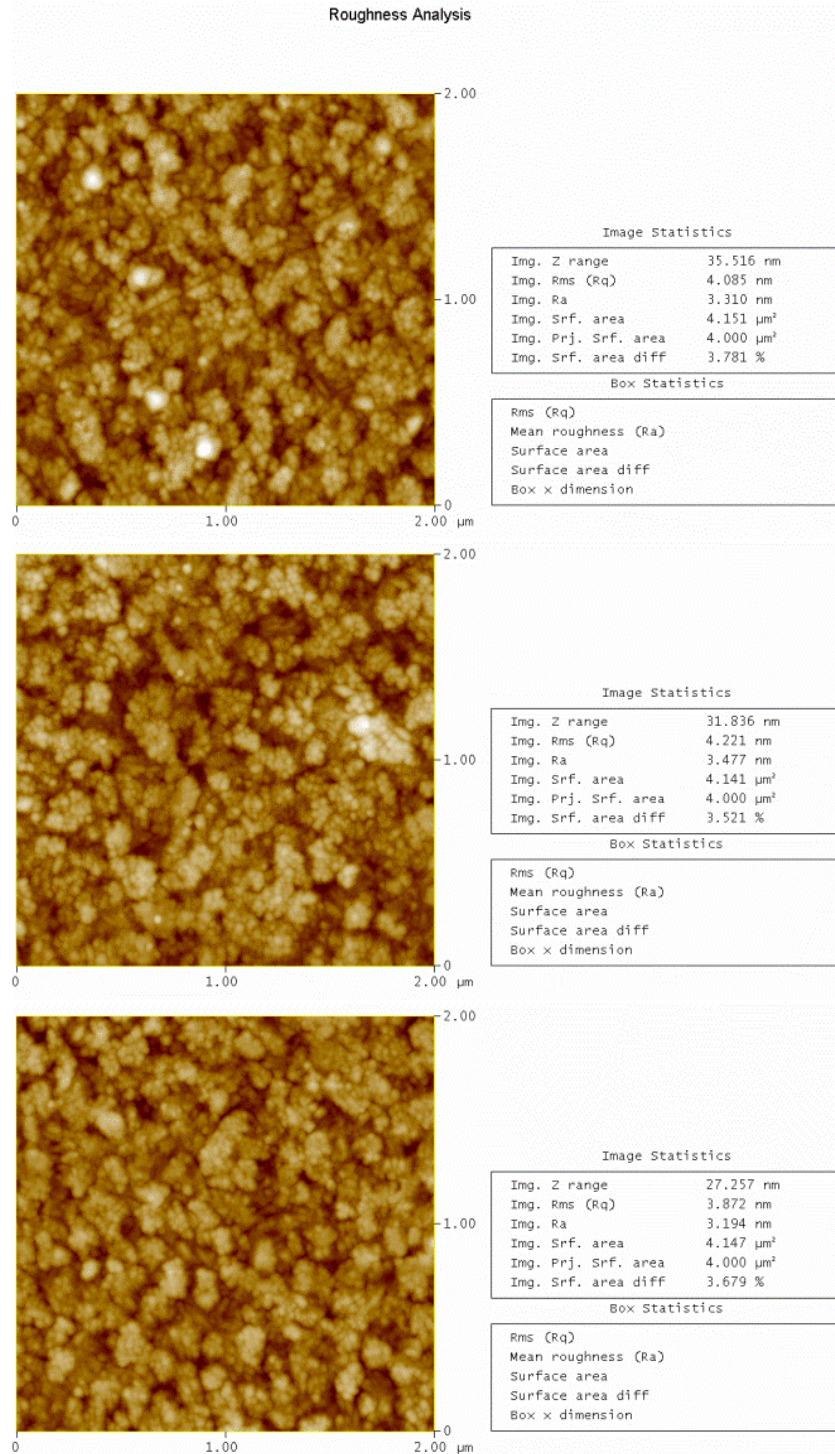


Figure 38-  $2\ \mu\text{m} \times 2\ \mu\text{m}$  AFM tapping scans of ITO samples for roughness analyses.

# BIBLIOGRAPHY

1. International Energy Agency, World Energy Outlook (2013).
2. U.S. Energy Information Administration (EIA), International Energy Outlook (2013).
3. International Energy Agency, Redrawing the Energy Climate Map: World Energy Outlook Special Report (2013).
4. European Commission, PV Status Report (2013).
5. International Energy Agency, Key World Energy Statistics (2013).
6. Basic Energy Science (BES) Workshop, Basic Research Needs for Solar Energy Utilization (2005).
7. Fthenakis, V., Sustainability of photovoltaics: The case for thin-film solar cells. *Renewable and Sustainable Energy Reviews* **13**, 2746 (2009).
8. Chuang, C. H. M., Brown, P. R., V.Bulović & Bawendi, M. G., Improved performance and stability in quantum dot solar cells through band alignment engineering. *Nature* **13**, 796 (2014).
9. Fella, C. M., Romanyuk, Y. E. & Tiwari, A. N., Technological status of  $\text{Cu}_2\text{ZnSn}(\text{S},\text{Se})_4$  thin film solar cells. *Solar Energy Materials and Solar Cells* **119**, 276 (2013).
10. Dasgupta, U., Saha, S. K. & Pal, A. J., Fully-depleted pn-junction solar cells based on layers of  $\text{Cu}_2\text{ZnSnS}_4$  (CZTS) and copper-diffused  $\text{AgInS}_2$  ternary nanocrystals. *Solar Energy Materials and Solar Cells* **124**, 79 (2014).
11. McGehee, M. D., Materials science: Fast-track solar cells. *Nature* **501**, 323 (2013).
12. Y. W. Su, S. C. L. H. W., Organic photovoltaics. *Materials today* **15**, 554 (2012).

13. National Renewable Energy Laboratory, National Renewable Energy Laboratory Website, Available at <http://www.nrel.gov>.
14. Krebs, F. C., Fabrication and processing of polymer solar cells: A review of printing and coating techniques. *Solar Energy Materials & Solar Cells* **93**, 394 (2009).
15. Shirakawa, H., Louis, E. J., MacDiarmid, A. G., Chiang, C. K. & Heeger, J. A., Synthesis of electrically conducting organic polymers: halogen derivatives of polyacetylene, (CH)<sub>x</sub>. *Journal of the Chemical Society: Chemical Communications*, 578 (1977).
16. Zoppi, R. A. & Paoli, M. A. D., Aplicações tecnológicas de polímeros intrínsecamente condutores: perspectivas atuais. *Química nova* **16**, 560 (1993).
17. Brown, Lemay & Bursten, *Chemistry: The central science*, 7th ed. (Prentice Hall, Upper Saddle River, NJ. USA., 1997).
18. Stella, L., Nano-bio spectroscopy group, Available at [http://nano-bio.ehu.es/files/pa\\_o.pdf](http://nano-bio.ehu.es/files/pa_o.pdf) (2011).
19. S. Ikehata et al. *Phys. Rev. Lett.* **45**, 423 (1980).
20. M. Peo et al. *Solid State Commun.* **35**, 119 (1980).
21. Scott, J. C., M, Krounbi, Pfluger, P. & Street, G. B. *Phys. rev. B: Condens. Matter* **28**, 2140 (1983).
22. Strobl, G. R., *The physics of Polymers: Concepts for Understanding Their Structures and Behavior*, 3rd ed. (Springer, 2007).
23. Bredas, J. L. & Street, G. B., Polarons, bipolarons and solitons in conducting polymers. *Acc. Chem. Res.* **18**, 309 (1985).
24. Brazovzkii, S. & Kirova, N., Physical theory of excitons in conductin polymers. *Chem. Soc. Rev.* **39**, 2453 (2010).
25. Becquerel, A. E., Recherches sur les effets de la radiation chimique de la lumiere solaire au moyen des courants electriques. *Comptes Rendus de L'Academie des Sciences* **9**, 145 (1839).
26. Adams, W. G. & Day, R. E., The Action of Light on Selenium. *Proceedings of the Royal Society (London)* **A25**, 113 (1877).
27. Fritts, C. E., On a New Form of Selenium Photocell. *Proc. Am. Assoc. Adv. Sci.* **33**, 97 (1883).
28. Nelson, J., *The physics of solar cells*, 1st ed. (Imperial college, London, 2003).
29. Gregg, B. A. & Hanna, M. C., Comparing organic to inorganic photovoltaic cells: Theory, experiment and simulation. *J. Appl. Phys.* **93**, 3605 (2003).
30. Hains, A. W., Liang, Z., Woodhouse, M. A. & Gregg, B. A., Molecular Semiconductors in Organic

- Photovoltaic Cells. *Chem. Rev.* **110**, 6689 (2010).
31. Kittel, C., *Introduction to solid state physics* (John Wiley & Sons Inc. , New York, U.S., 1996).
  32. Green, M. A., Improved value for the silicon free exciton binding energy. *AIP Advances* **3**, 112104 (2013).
  33. Nam, S. B., Reynolds, D. C., Litton, C. W., Almassy, R. J. & Collins, T. C., Free-exciton energy spectrum in GaAs. *Phys. Rev. B* **13**, 761 (1976).
  34. Rand, B. P., Genoe, J., Heremans, P. & Poortmans, J., Solar cells utilizing small molecular weight organic semiconductors. *Prog. Photovolt: Res. Appl.* **15**, 659 (2007).
  35. Coropceanu, V. *et al.*, Charge Transport in Organic Semiconductors. *Chem. Rev.* **107**, 926 (2007).
  36. Günes, S., Neugebauer, H. & Sariciftci, N. S., Conjugated Polymer-Based Organic Solar Cells. *Chem. Rev.* **107**, 1324 (2007).
  37. Kraabel, B., Lee, C. H., Mcbranch, D., Moses, D. & Sariciftci, N. S., Ultrafast photoinduced electron transfer in conducting polymer buckminsterfullerene composites. *Chem. Phys. Lett.* **213**, 389 (1993).
  38. Hoppe, H. & Sariciftci, N. S., *Polymer solar cells*, 1st ed. (Springer, Berlin, 2007).
  39. Schottky, W. H., Halbleitertheorie der Sperrschicht (Semiconductor theory of the barrier layer). *Die Naturwissenschaften* **26**, 843 (1938).
  40. Brabec, C. J., Sariciftci, N. S. & Hummelen, J. C., Plastic solar cells. *Adv. Funct. Mater.* **11**, 15 (2001).
  41. Tang, C. W., Two layer organic photovoltaic cell. *Appl. Phys. Lett.* **48**, 183 (1986).
  42. Yu, G., Gao, J., Hummelen, J. C., Wudl, F. & Heeger, A. J., Polymer Photovoltaic Cells: Enhanced Efficiencies via a Network of Internal Donor-Acceptor Heterojunctions. *Science* **270**, 1789 (1995).
  43. Heeger, A. J., Bulk Heterojunction Solar Cells: Understanding the Mechanism of Operation. *Adv. Mater.* **26**, 10 (2014).
  44. Cowan, S. R., Roy, A. & Heeger, A. J., Recombination in polymer-fullerene bulk heterojunction solar cells. *Phys. Rev. B* **82**, 245207 (2010).
  45. Granqvist, C. G. & Hultaker, A., Transparent and conducting ITO films: new developments and applications. *Thin Solid Films* **411**, 1 (2002).
  46. Ginley, D. S. & Bright, C., Transparent Conducting Oxides. *MRS Bull.* **25**, 15 (2000).
  47. Salvadori, M. C., Laboratório de Filmes Finos - IFUSP, Available at <http://fap.if.usp.br/~lff/mepiuid.html> (2014).
  48. Salvadori, M. C. *et al.*, Low cost ion implantation technique. *Appl. Phys. Lett.* **101**, 224104 (2012).
  49. Anders, A. & Yushkov, G. Y. *J. Appl. Phys.* **91**, 4824 (2002).

50. Tabacniks, M. H., LAMFI - IFUSP, Available at <http://www2.if.usp.br/~lamfi/pixe&rbs.pdf>.
51. Möller, W. & Eckstein, W., Nucl. Instrum. Meth. *Phys. Res. B* **2**, 814 (1984).
52. Möller, W., Eckstein, W. & Biersack, J. P. *Comput. Phys. Commun.* **51**, 355 (1988).
53. Reference Solar Spectral Irradiance: Air Mass 1.5, Available at <http://rredc.nrel.gov/solar/spectra/ami.5/#about>.
54. Gan, Q., Bartoli, F. J. & Kafafi, Z. H., Plasmonic-Enhanced OPV: Breaking the 10% Efficiency barrier. *Adv. Mater.* **25**, 2385 (2013).
55. Wang, C. D. *et al.*, Optical and electrical effects of gold nanoparticles in the active layer of polymer solar cells. *J. Mater. Chem.* **22**, 1206 (2012).
56. Chen, F. C. *et al.*, Plasmonic-enhanced polymer photovoltaic devices incorporating solution-processable metal nanoparticles. *App. Phys. Lett.* **95**, 13305 (2009).
57. Lee, J. H., Park, J. H., Kim, J. S., Lee, D. Y. & Cho, K., High efficiency polymer solar cells with wet deposited plasmonic gold nanodots. *Organic electronics* **10**, 416 (2009).
58. Morfa, A. J. & Rowlen, K. L., Plasmon-enhanced solar energy conversion in organic BHJ photovoltaics. *Appl. Phys. Lett.* **92**, 13504 (2008).
59. Fung, D. S. *et al.*, Optical and electrical properties of efficiency enhanced polymer solar cells with Au nanoparticles in the PEDOT:PSS layer. *J. Mater. Chem.* **21**, 16349 (2011).
60. Ardestani, S. S., Ajeian, R., Badrabad, M. N. & Tavakkoli, M., Improvement in stability of bilayer organic solar cells using an ultra-thin Au layer. *Sol. Energy Mater. Sol. Cells* **111**, 107 (2013).
61. Yambem, S. D., Liao, K. S., Alley, N. J. & Curran, S. A., Stable organic photovoltaics using Ag thin film anodes. *J. Mater. Chem.* **22**, 6894 (2012).
62. Gholamkhash, B. & Holdcroft, S., Enhancing the durability of polymer solar cells using gold nanodots. *Sol. Energ. Mat. Sol. C.* **95**, 3106 (2011).
63. C. D. Wang, W. C. H. C., Efficient hole collection by introducing ultra-thin UV-ozone treated Au in polymer solar cells. *Sol. Energ. Mater. & Sol. C.* **95**, 904 (2011).
64. Cheng, C. E., Pei, Z., Hsu, C. C., Chang, C. S. & Chien, F. S., Hole transit in P<sub>3</sub>HT:PCBM solar cells with embedded gold nanoparticles. *Sol. Energ. Mat. Sol. Cells* **121**, 80 (2014).
65. Betz, U., K.Olsson, M., Marthy, J., Escolá, M. F. & Atamny, F., Thin films engineering of indium tin oxide: Large area flat panel displays application. *Surf. Coat. Tech.* **200**, 5751 (2006).
66. Stepanov, A. L., Hole, D. E. & Townsend, P. D., Formation of silver nanoparticles in soda-lime silicate glass by ion implantation near room temperature. *J. Non-Crystalline Solids* **260**, 65 (1999).
67. Kumar, A., Sista, S. & Yang, Y., Dipole induced anomalous S-shape I-V curves in polymer solar

- cells. *J. Appl. Phys.* **105**, 94512 (2009).
68. Gupta, D., Bag, M. & Narayan, K. S., Correlating reduced fill factor in polymer solar cells to contact effects. *Appl. Phys. Lett* **92**, 93301 (2008).
69. Wang, J. C., Ren, X. C., Shi, S. Q., Leung, C. W. & Chan, P. K. L., Charge accumulation induced S-shape J-V curves in bilayer heterojunction organic solar cells. *Org. Electron.* **12**, 880 (2011).
70. Huh, Y. H., Park, B. & Hwang, I., Investigating the origin of S-shaped photocurrent-voltage characteristics of polymer:fullerene BHJ organic solar cells. *J. Appl. Phys.* **115**, 124504 (2014).
71. Sullivan, P. & Jones, T. S., Pentacene/fullerene (C60) heterojunction solar cells: Device performance and degradation mechanisms. *Org. Electron.* **9**, 656 (2008).
72. Jin, H. *et al.*, Polymer–Electrode Interfacial Effect on Photovoltaic Performances in Poly(3-hexylthiophene):Phenyl-C61-butyric Acid Methyl Ester Based Solar Cells. *J. Phys. Chem. C* **113**, 16807 (2009).
73. Tress, W. *et al.* *Appl. Phys. Lett.* **98**, 63301 (2011).
74. Glatthaar, M. *et al.*, Efficiency limiting factors of organic bulk heterojunction solar cells identified by electrical impedance spectroscopy. *Sol. Ener. Mater. Sol. Cells* **91**, 390 (2007).
75. Villers, B. T., Tassone, C. J., Tolbert, S. H. & Schwartz, B. J., Improving the Reproducibility of P3HT:PCBM Solar Cells by Controlling the PCBM/Cathode Interface. *J. Phys. Chem. C* **113**, 18978 (2009).
76. Koch, N., Vollmer, A. & Elschner, A., Influence of water on the work function of conducting poly(3,4-ethylenedioxythiophene)/poly(styrenesulfonate). *Appl. Phys. Lett.* **90**, 43512 (2007).
77. Jorgensen, M., Norrman, K. & Krebs, F. C., Stability/degradation of polymer solar cells. *Sol. Energ. Mat. Sol. Cells* **92**, 686 (2008).
78. Yang, H. B., Song, Q. L., Gong, C. & Li, C. M., The degradation of indium tin oxide/pentacene/fullerene/tris-8-hydroxy-quinolinato aluminum/aluminum heterojunction organic solar cells: By oxygen or moisture? *Sol. Energ. Mat. Sol. Cells* **94**, 846 (2010).
79. Brabec, C. J. *et al.*, Origin of the Open Circuit Voltage of Plastic Solar Cells. *Adv. Funct. Mater.* **11**, 374 (2001).
80. Veeco Instruments, A practical guide to SPM (2005).

